Feature Extraction of Frequency-Mapping-Based Resonance Suppression in PMSM Drives With Low DC-Link Capacitance and Inductance

Runfeng Gao, Dawei Ding, *Member, IEEE*, Gaolin Wang, *Senior Member, IEEE*, Qiwei Wang, *Member, IEEE*, Guoqiang Zhang, *Senior Member, IEEE*, and Dianguo Xu, *Fellow, IEEE*

***Abstract*—For the electrolytic capacitorless permanent magnet synchronous motor drives with low dc-link inductance, the increase of the resonant frequency and the complex coupling between the grid- and dc-side currents result in the performance reduction of the active damping method. This article proposes a suppression strategy based on the feature extraction of the grid current harmonics from frequency mapping. With the high-to-low frequency mapping, the low-frequency feature signals of grid current harmonics are applied to characterize the high-frequency resonance, which reduce the sampling and update errors caused by the higher resonant frequency. On the basis, the closed-loop control of the low-frequency feature signal is adopted to reshape the impedance relationship between the grid current and rectified voltage. Therefore, the harmonics of the grid current can be decoupled from the dc-side current, and the high-frequency resonance of the grid current can be directly controlled, which realizes resonance suppression in the low dc-link inductance drives. Experimental results verify the effectiveness of the proposed suppression strategy.**

***Index Terms*—Electrolytic capacitorless drives, feature signal, frequency mapping, high-frequency resonance, low dc-link inductance.**

I. Introduction

A PERMANENT magnet synchronous motor (PMSM) is widely applied in transportation and industrial conditions. The voltage source inverters have gradually become the main driving method [1]. Large aluminum electrolytic capacitors are usually utilized as the energy buffers to stabilize the dc-link voltage [2], [3]. However, the lifetime of the electrolytic capacitor is closely related to the environment temperature, which causes the failure of the whole drive system. In order to improve the system reliability, applying slim-film capacitors in the dc link can extend the system lifetime and reduce the system cost [4].

Although the drive systems with small dc-link capacitors have many advantages, there exist several control challenges. Due to the reduction of the energy storage capacity, the dc-link voltage cannot maintain a constant value, which deteriorates the energy coupling between the grid side, dc link, and motor side. The major issues are mainly divided into two aspects: performance decay at the motor side and the grid side [5]. As for the motor side, the inverse proportional correlation can be seen between the dc-link voltage utilization rate and torque ripple constraints in the high-speed region [6]. The energy regulation at the motor side is one of the key research points for the drive system without electrolytic capacitors. The power quality issues at the grid side are usually caused by *LC* resonance [7]. The dc-link inductor is in series with the dc link to suppress the high-frequency noise. *LC* resonance causes the distortion of the grid and dc-link waveforms. The inverter system with the current loop can be regarded as a constant power load, which means that the negative input impedance aggravates *LC* resonance [8]. To improve the power density and reduce the system cost, the dc-link inductance is further reduced, which increases the sampling and updating errors. The complex coupling between the grid- and dc-side current also affects the harmonic suppression ability of the strategy [9].

LC resonance is a hot issue in power electronics, and its solutions can be divided into two categories: the hardware topology methods and software algorithms methods [10], [11]. For hardware-based solutions, the passive components were in series or parallel with the dc-link inductor or capacitor to suppress the resonance [12]. In [13], a controlled *LC* resonance compensator was designed to be in parallel with the dc link, which suppressed the grid harmonics by absorbing the power near the resonant frequency. On the basis, the model-predictive strategy was combined to further improve the control performance [14]. In [15], a half-bridge controlled rectifier and a four-switch three-phase inverter were applied in the ac–dc–ac system, which adjusted the shape of grid currents according to the harmonic requirements. However, the aforementioned methods were realized through adding additional power electronic devices, which increases the volume and cost of the system.

Received 8 July 2024; revised 24 September 2024; accepted 8 November 2024. Date of publication 19 November 2024; date of current version 28 January 2025. This work was supported in part by the National Natural Science Foundation of China under Grant 52207042 and Grant 52125701, in part by the Delta Power Electronics Science and Education Development Program of Delta Group under Grant DREG2023005, in part by the Young Elite Scientists Sponsorship Program of the China Association for Science and Technology under Grant 2023QNRC001, in part by the Natural Science Foundation of Heilongjiang Province under Grant LH2023E047, in part by the Heilongjiang Postdoctoral Fund under Grant LBH-Z220022, and in part by the Fundamental Research Funds for the Central Universities under Grant HIT.BRET.2021007. Recommended for publication by Associate Editor P. Karamanakos. *(Corresponding author: Qiwei Wang.)*

The authors are with the School of Electrical Engineering and Automation, Harbin Institute of Technology, Harbin 150001, China (e-mail: 1160800915@stu.hit.edu.cn; dingdawei@hit.edu.cn; wgl818@hit.edu.cn; wqwhit@hit.edu.cn; zhgq@hit.edu.cn; xudiang@hit.edu.cn).

Color versions of one or more figures in this article are available at https://doi.org/10.1109/TPEL.2024.3501476.

Digital Object Identifier 10.1109/TPEL.2024.3501476

Software algorithm methods have the advantages of flexibility and low cost, which can also be divided into two categories. Conventional suppression methods are suitable for the drive system with large dc-link inductance [16], [17]. In [18], a voltage-modulation-based strategy was defined as "virtual positive impedance" to improve the drive system stability, which applied the rectified voltage to suppress the harmonics near the resonant frequency. In [19], a virtual admittance method with low power disturbance was utilized by obtaining the dc-link inherent harmonics, which increased the damping of the whole system for resonance suppression [20]. The realization of the aforementioned damping methods required extracting *LC* resonance information from the dc side, which means that the suppression ability was reduced in the drive systems with less obvious resonance. The drive systems with low inductance or without the inductor have higher demands on resonance suppression [21]. In [22], the motor torque and fast voltage feedforward control were applied to improve the grid current quality in the drives without the dc-link inductor. As for the elimination of the dc-link inductor, the grid harmonics near the switching frequency caused by the inverter modulation are difficult to be suppressed. In [23], a strategy based on the harmonic regulation of rectified current was applied in the drive system with low dc-link inductance, which improved the grid quality by adding the resonant component to field-oriented control (FOC). However, the increase of the resonant frequency was not considered, which introduces additional errors in the harmonic extraction. In [24], the phase delay and amplitude decay of resonance information were compensated to further enhance the suppression effectiveness. Except for the dc-side current harmonics, the mean value of the dc-side current contributes to the generation of the grid current, which results in the severe coupling between grid- and dc-side currents [25], [26]. The current coupling and high resonant frequency increase the difficulty of suppressing the resonance, which limit the reduction in the cost and volume of drive systems [27], [28].

In this article, a resonance suppression strategy based on the feature extraction from the frequency mapping is proposed. The system error caused by the increase of the resonant frequency is analyzed. The complex coupling between the grid- and dc-side currents further reveals the limitations of the active damping method realized by extracting the resonance harmonic directly. The feature signals of the grid current harmonics are extracted with the average value and harmonics of dc-side current to decouple the grid- and dc-side currents. With the high-to-low frequency mapping, the low-frequency feature signals are applied to characterize the current harmonic amplitude near the high resonant frequency, and the closed-loop control is further performed to achieve effective suppression. The proposed method constructs a control loop of low-frequency feature signal, which reshapes the impedance near the high resonant frequency. Hence, the problem of suppression difficulty at high resonant frequencies can be solved. The switching frequencies $\omega_{\rm s}$ and resonant frequencies $\omega_{\rm re}$ of the existing suppression methods are shown in Table I.

According to recent research, the ratio $\omega_{\rm re}/\omega_s$ of 0.15 can be regarded as the high-frequency resonance. Hence, the switching frequency is set as 8 kHz under the resonant frequency of 1258 Hz.

TABLE I
SWITCHING AND RESONANT FREQUENCIES OF RESONANCE SUPPRESSION METHOD

Methods	$\omega_{\rm s}$	$\omega_{\rm re}$	*Ratios* $\omega_{\rm re}/\omega_{\rm s}$
Improved topologies	10 kHz	300–1850 Hz	0.03–0.18
Existing algorithms for low-frequency resonance [16], [17], [18], [19]	8–10 kHz	503–581 Hz	0.054–0.072
Existing algorithms for high-frequency resonance [23], [24], [25], [26]	6–10 kHz	900–1779 Hz	0.15–0.18
Proposed method	8 kHz	1258 Hz	0.15

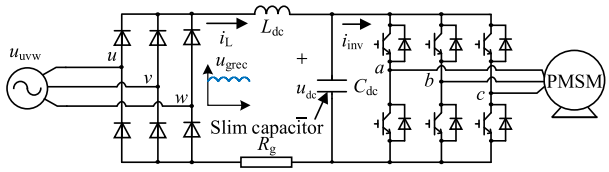

Fig. 1. Topology of the PMSM drive with the small dc-link capacitor.

II. Analysis of the Resonant Component of Grid Current in Motor Drives With Low DC-Link Inductance

A. Impedance Model With Low DC-Link Inductance

The topology of the electrolytic capacitorless drives with low dc-link inductance is shown in Fig. 1. Due to the low dc-link capacitance, the dc-link voltage $u_{\rm dc}$ and dc-side current i_L can be expressed as

$$\begin{cases} u_{\rm dc} = U_{\rm dc,0} + \sum_{k=1}^{\infty} u_{{\rm dc},k} = U_{\rm dc,0} \\ \qquad + \sum_{k=1}^{\infty} U_{{\rm dc},k} \sin\left(6k\omega_g t + \varphi_{{\rm dc}k}\right) \\ i_L = I_{L,0} + \sum_{k=1}^{\infty} i_{L,k} = I_{L,0} \\ \qquad + \sum_{k=1}^{\infty} I_{L,k} \sin\left(6k\omega_g t + \varphi_{Lk}\right) \end{cases} \tag{1}$$

where $U_{\rm dc,0}$ and $u_{{\rm dc},k}$ are the mean value and the kth harmonic of the dc-link voltage, respectively. $U_{{\rm dc},k}$ and $\varphi_{{\rm dc}k}$ are the amplitude and the phase of $u_{{\rm dc},k}$, respectively. $I_{L,0}$ and $i_{L,k}$ are the mean value and the kth harmonic of the dc-side current, respectively. $I_{L,k}$ and φ_{Lk} are the amplitude and the phase of $i_{L,k}$, respectively. ω_g is the grid angular frequency.

From [19], the rectified voltage u_{grec} can be expressed as

$$u_{grec} = 3U_g \left[1 - \sum_{k=1}^{\infty} 2\cos(6k\omega_g t + 6k\varphi)/(36k^2 - 1)\right]/\pi \tag{2}$$

where U_g and φ are the amplitude and the phase of the line voltage, respectively.

In order to analyze the impact of *LC* resonance on the grid current harmonics accurately, the impedance model of the drive system with low dc-link inductance is built. As can be seen in Fig. 2, the system input is the rectified voltage u_{grec}, and

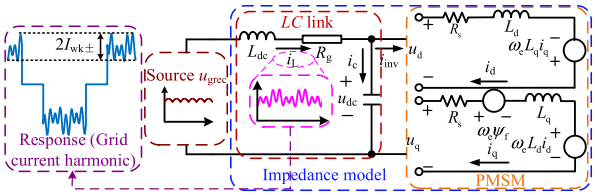

Fig. 2. Impedance model with the drive with the small dc-link capacitor.

the output is the grid current harmonics i_{wk-} and i_{wk+} at the frequency of $(6k-1)\omega_g$ and $(6k+1)\omega_g$, whose amplitudes are I_{wk-} and I_{wk+}, respectively.

According to Fig. 1 and [19], the dc-side current is directly related to the grid current, which means that the grid current harmonics can be obtained by $\Delta i_L/\Delta u_{grec}$. Δi_L and Δu_{grec} are the variations of the dc-side current and the rectified voltage, respectively. The amplitude and phase errors caused by the sampling process (sampling time is T_s) cannot be ignored under the high-frequency resonance, whose transfer function $\boldsymbol{G}_h$ is

$$\boldsymbol{G}_h = (1-e^{-sT_s})/sT_s. \tag{3}$$

According to [6], $\boldsymbol{W}_d$ and $\boldsymbol{W}_q$ are defined as the transfer function from the dc-link voltage variation $\Delta u_{\rm dc}$ to the current variations Δi_d and Δi_q in dq-axes, which are denoted as

$$\begin{bmatrix}\boldsymbol{W}_d\\ \boldsymbol{W}_q\end{bmatrix} = \frac{1}{\Delta u_{\rm dc}}\begin{bmatrix}\Delta i_d\\ \Delta i_q\end{bmatrix} = \frac{(1-e^{-1.5sT_s})/U_{\rm dc,0}}{\boldsymbol{A}_{2q}\boldsymbol{A}_{1d}-\boldsymbol{A}_{2d}\boldsymbol{A}_{1q}} \times \begin{bmatrix}U_{d\rm ref,0}\boldsymbol{A}_{2q}-U_{q\rm ref,0}\boldsymbol{A}_{1q}\\ U_{q\rm ref,0}\boldsymbol{A}_{1d}-U_{d\rm ref,0}\boldsymbol{A}_{2d}\end{bmatrix}. \tag{4}$$

$$\begin{bmatrix}\boldsymbol{A}_{1d} & \boldsymbol{A}_{1q}\\ \boldsymbol{A}_{2d} & \boldsymbol{A}_{2q}\end{bmatrix} = \begin{bmatrix}R_s+L_ds & -\omega_eL_q\\ \omega_eL_d & R_s+L_qs\end{bmatrix} + e^{-sT_s}\boldsymbol{G}_h\begin{bmatrix}\boldsymbol{G}_d & 0\\ 0 & \boldsymbol{G}_q\end{bmatrix}. \tag{5}$$

In (4), $U_{d,\rm qref,0}$ is the reference voltages in dq-axes. In (5), $L_{d,q}$, $\boldsymbol{G}_{d,q}$, R_s, and ω_e are the inductances in dq-axes, the transfer functions of the current controllers in dq-axes, the stator resistance, and the motor frequency, respectively.

$\boldsymbol{K}_m$ is defined as the transfer function between the dc-side current and the rectified voltage, which is derived as

$$\boldsymbol{K}_m = \Delta i_L/\Delta u_{\rm grec} = 1/[1/(\boldsymbol{Y}_m + C_{\rm dc}s) + (L_{\rm dc}s + R_g)] \tag{6}$$

where $L_{\rm dc}$, $C_{\rm dc}$, and R_g are the dc-link inductance, the dc-link capacitance, and the line resistance, respectively.

$\boldsymbol{Y}_m$ is the transfer function of the inverter input admittance

$$\begin{aligned}\boldsymbol{Y}_m = {} & [-I_{L,0} + 1.5\boldsymbol{W}_d(U_{d,0} + \omega_eL_dI_{q,0} + L_dI_{d,0}s \\ & + I_{d,0}R_s) + 1.5\boldsymbol{W}_q(U_{q,0} - \omega_eL_qI_{d,0} \\ & + L_qI_{q,0}s + I_{q,0}R_s)]/U_{\rm dc,0}\end{aligned} \tag{7}$$

where $U_{dq,0}$ and $I_{dq,0}$ are the average values of the actual voltages and currents in dq-axes, respectively.

$\Delta\boldsymbol{K}_m$ and the resonant frequency $\omega_{\rm re}$ are defined as

$$\Delta\boldsymbol{K}_m = \boldsymbol{K}_m - \boldsymbol{K}_{m,id}, \omega_{\rm re} = 1/2\pi\sqrt{L_{\rm dc}C_{\rm dc}} \tag{8}$$

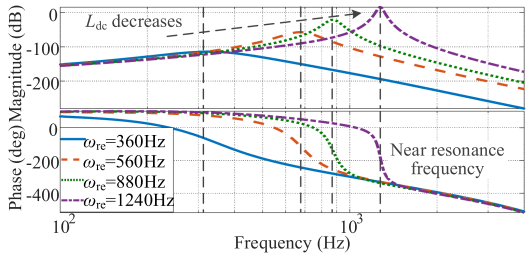

Fig. 3. Block diagram of $\Delta\boldsymbol{K}_m$ under different values of $\omega_{\rm re}$.

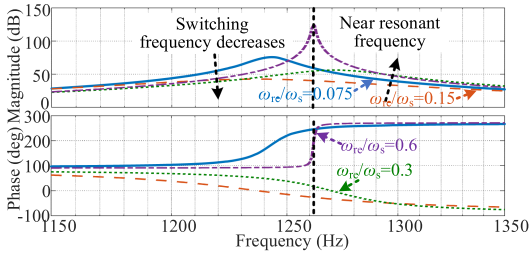

Fig. 4. Bode diagrams of $\boldsymbol{K}_m$ under different values of switching frequency ω_s.

where $\boldsymbol{K}_{m,\rm id}$ is the transfer function of $\Delta i_L/\Delta u_{\rm grec}$ under the ideal condition ($T_s = 0$). From (8), the sampling and updating errors of the harmonics caused by LC resonance increase as $\omega_{\rm re}$ increases [24]. $\Delta\boldsymbol{K}_m$ can be applied to analyze the deviations of the dc-side current caused by the digital algorithm, whose Bode diagrams are shown in Fig. 3. As $\omega_{\rm re}$ increases from 360 to 1240 Hz, the amplitude and phase deviations near the resonant frequency vary from –114 dB and –68° to 4 dB and –184°, respectively. The reduction of $L_{\rm dc}$ increases the errors of the dc-side current harmonics near $\omega_{\rm re}$, which enhances the difficulty of extracting the resonance information of grid current directly.

In this article, the resonant frequency $\omega_{\rm re}$ is 1258 Hz. Under different values of the ratio $\omega_{\rm re}/\omega_s$, the Bode diagrams of K_m are shown in Fig. 4. The influence of the sampling and updating delay on the resonant component decreases with the increase of switching frequency.

As the ratio $\omega_{\rm re}/\omega_s$ decreases to 0.15, the magnitude of $\boldsymbol{K}_m$ near $\omega_{\rm re}$ is reduced from 87 to 41 dB, which means that the moderate increase of the switching frequency can suppress LC resonance in the dc-side current and the grid current. However, $|\boldsymbol{K}_m|$ near $\omega_{\rm re}$ increases to 62 dB as the switching frequency is further set as 17 kHz. Hence, setting the switching frequency as 8 kHz ($\omega_{\rm re}/\omega_s = 0.15$) contributes to the resonance suppression.

B. *Grid Current Harmonics Caused by* LC *Resonance*

In order to obtain the grid current harmonics affected by LC resonance, the relationship between the grid- and dc-side currents needs to be further analyzed. The phase relationship among the grid current, the dc-side current, and the rectified voltage is shown in Fig. 5. The w-phase grid current i_w contains the harmonics i_{wk-} and i_{wk+} at $(6k-1)\omega_g$ and $(6k+1)\omega_g$

$$i_{wk\pm} = a_k\cos(6k\pm1)(\omega_gt+\varphi) + b_k\sin(6k\pm1)(\omega_gt+\varphi)$$

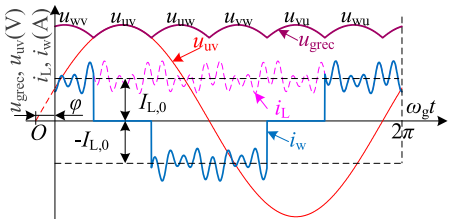

Fig. 5. Phase relationship among i_w, i_L, and u_{grec}.

$$= I_{wk\pm}\sin\left[(6k\pm1)(\omega_g t+\varphi)+\varphi_{wk\pm}\right] \tag{9}$$

where $\varphi_{wk\pm}$ is the phase difference between the grid current $i_{wk\pm}$ and the rectified voltage harmonics related to $6k\omega_g$

$$\begin{cases} a_k = \pm\frac{2\sqrt{3}}{\pi}\left\{\frac{I_{L,0}}{6k\pm1}-\sum_{k_1=1}^{\infty}\frac{(6k\pm1)I_{L,k_1}\sin\varphi_{erk_1}}{\left[(6k_1)^2-(6k\pm1)^2\right]}\right\} \\ b_k = \mp\sum_{k_1=1}^{\infty}12\sqrt{3}k_1 I_{L,k_1}\cos\varphi_{erk_1}\Big/ \\ \qquad \pi\left[(6k_1)^2-(6k\pm1)^2\right] \end{cases}. \tag{10}$$

In (10), φ_{erk} is the phase difference between the dc-side current $i_{L,k}$ and the rectified voltage harmonics at $6k\omega_g$

$$\varphi_{erk} = \varphi_{Lk} - 6k\varphi = \angle \boldsymbol{K}_{mk} - \pi/2 \tag{11}$$

where $\boldsymbol{K}_{mk}$ represents $\boldsymbol{K}_m(j6k\omega_g)$.

From (10), the grid harmonics i_{wk-} and i_{wk+} are closely related to the mean value $I_{L,0}$ and harmonics $i_{L,k}$ of the dc-side current at $6k\omega_g$, which means that the harmonics of grid current is coupled with those of dc-side current. Hence, (9) can be rewritten as

$$\begin{aligned} i_{wk\pm} = i_{mk\pm} + i_{hk\pm} = 2\sqrt{3}\{&\pm I_{L,0}\cos(6k\pm1) \\ &\times(\omega_g t+\varphi)/(6k\pm1) \\ &+ M_{6k\pm}I_{L,k}\sin\left[(6k\pm1)(\omega_g t+\varphi)+\varphi_{6k\pm}\right]/ \\ &(12k\pm1)\}/\pi \end{aligned} \tag{12}$$

where $i_{mk\pm}$ and $i_{hk\pm}$ are the grid current harmonics related to the mean value and harmonics of the dc-side current, respectively. The amplitude of $i_{mk\pm}$ is less influenced by *LC* resonance.

In (12), $M_{6k\pm}$ is the amplitude ratio between $i_{hk\pm}$ and $i_{L,k}$. $\varphi_{6k\pm}$ is the phase difference between $i_{hk\pm}$ and the rectified voltage harmonics at the frequency of $6k\omega_g$

$$\begin{cases} M_{6k\pm} = \sqrt{36k^2+(\pm12k+1)\sin^2\varphi_{erk}} \\ \varphi_{6k\pm} = \arcsin\left[(6k\pm1)\sin\varphi_{erk}/M_{6k\pm}\right] \end{cases}. \tag{13}$$

From (12), the amplitude $I_{wk\pm}$ and phase $\varphi_{wk\pm}$ of the grid current harmonics can be expressed as

$$\begin{cases} I_{wk\pm} = \frac{2\sqrt{3}}{\pi}\sqrt{\left[\frac{6M_{6k\pm}|\boldsymbol{K}_{mk}|U_g\sin\varphi_{6k\pm}}{\pi(36k^2-1)(12k\pm1)}\pm\frac{I_{L,0}}{6k\pm1}\right]^2+\left[\frac{6M_{6k\pm}|\boldsymbol{K}_{mk}|U_g\cos\varphi_{6k\pm}}{\pi(36k^2-1)(12k\pm1)}\right]^2} \\ \varphi_{wk\pm} = \arcsin\frac{6M_{6k\pm}|\boldsymbol{K}_{mk}|U_g\cos\varphi_{6k\pm}}{\pi(36k^2-1)(12k\pm1)I_{wk\pm}} \end{cases}. \tag{14}$$

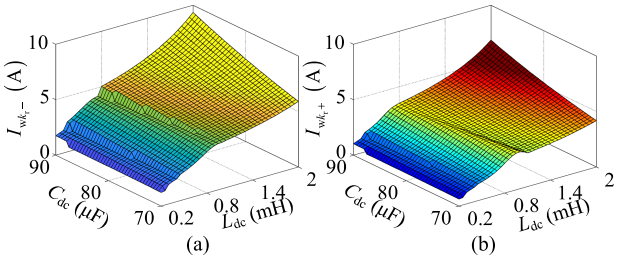

Fig. 6. Relationship between the grid current ripple and *LC* resonance under the output power of 5 kW. (a) At $(6k_r-1)\omega_g$. (b) At $(6k_r+1)\omega_g$.

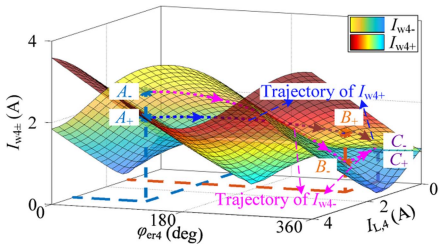

Fig. 7. Grid current amplitude near the resonant frequency under the variation of the amplitude and phase in the dc-side current.

From [24], the harmonic order k_r of the dc-side current, which is severely affected by *LC* resonance, is

$$k_r = \boldsymbol{R}(1/6\omega_g\sqrt{L_{\mathrm{dc}}C_{\mathrm{dc}}}) \tag{15}$$

where $\boldsymbol{R}(\cdot)$ rounds off the input to the nearest integer. The harmonic orders of the grid current, which are severely affected by *LC* resonance, are $(6k_r-1)$ and $(6k_r+1)$. *LC* resonance significantly increases current harmonics near ω_{re}.

The grid current harmonics near the resonant frequency under the output power of 5 kW are shown in Fig. 6, whose amplitudes decrease with the reduction of L_{dc} and C_{dc}. As L_{dc} and C_{dc} are lower than 0.6 mH and 75 μF, respectively, the harmonic amplitudes become less than 2 A. Compared with the drive system with large dc-link inductance, the difficulty of extracting the resonant component at the grid further increases.

Besides, the coupling between the grid harmonics $i_{wk\pm}$ and the mean value $I_{L,0}$ of the dc-side current also affects the accuracy of the grid resonance extraction. If only suppressing the resonant harmonic i_{L,k_r} of the dc-side current, such as the strategy in [19], the harmonic amplitude $I_{wk_r\pm}$ at the grid side may not decrease due to the change of the phase difference φ_{erk_r}. In this article, the resonant frequency is 1258 Hz. The harmonic amplitudes $I_{w4\pm}(k_r=4)$ under the variation of $i_{L,4}$ are shown in Fig. 7. Assuming that $A_\pm$ and $B_\pm$ are the points without and with the method, respectively, the dotted line shows the operation trajectory of $I_{w4\pm}$. I_{w4-} and I_{w4+} are suppressed by 1.90 and 0.60 A, respectively. As for *B*–, I_{w4-} is lower than the amplitude of i_{m4-}, which indicates that *LC* resonance suppresses I_{w4-} at this point. As $I_{L,4}$ is further reduced to 0 A, I_{w4-} is increased from 0.75 to 1 A, which worsen the grid quality. This means that the dc-side current harmonics is not suitable to characterize the *LC* resonance information of the grid current in the drive systems

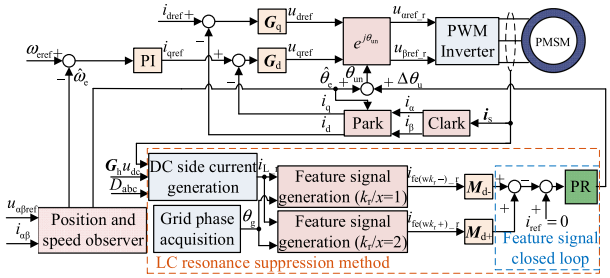

Fig. 8. Block diagram of the resonance suppression strategy based on the closed loop of the feature signal at dominated frequencies.

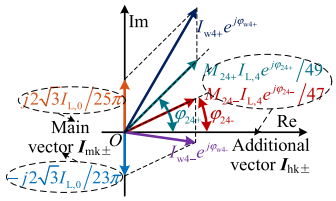

Fig. 9. Vector diagram of the grid current and the dc-side current harmonics.

with low inductance. Hence, the grid current improved method considering the influence of $I_{L,0}$ needs to be further researched.

III. Resonance Suppression Based on the Feature Extraction From Frequency Mapping

A. Feature Extraction Principle of Frequency Mapping

The block diagram of the resonance suppression strategy based on the closed loop of the feature signal is shown in Fig. 8. The dc-side current i_L is reconstructed with the motor current $\boldsymbol{i}_s$, duty cycle D_{abc}, and dc-link voltage. The compensated feature signals $i_{\mathrm{fe}(wk_r\pm)\_r}$ are generated by compensating the errors from the sampling and updating processes. x is the frequency coefficient, which adjusts the frequencies of $i_{\mathrm{fe}(wk_r-)\_r}$ and $i_{\mathrm{fe}(wk_r+)\_r}$ to $6\omega_g$ and $12\omega_g$, respectively. The output of the control loop is the voltage adjusting angle $\Delta\theta_u$, which is superimposed on the motor estimated position $\hat{\theta}_e$. The adjusted voltage angle is θ_{un}, which is involved in the inverse Park transformation of the voltage reference. The advantage of the closed loop of the grid feature signal is achieving the direct control of high-frequency resonance by decoupling the grid- and the dc-side currents.

The vector diagram of the grid current and the dc-side current is shown in Fig. 9. From (12), the vector $I_{wk\pm}e^{j\varphi_{wk\pm}}$ of grid harmonics is the sum of the vectors $\boldsymbol{I}_{mk\pm}$ and $\boldsymbol{I}_{hk\pm}$ related to the mean value and harmonics of dc-side current, respectively

$$I_{wk\pm}e^{j\varphi_{wk\pm}} = \frac{2\sqrt{3}}{\pi}\left[\pm j\frac{I_{L,0}}{6k\pm1} + \frac{M_{6k\pm}I_{L,k}}{12k\pm1}e^{j\varphi_{6k\pm}}\right]. \quad (16)$$

The ideal feature signals $i_{\mathrm{fe}(wk\pm)}$ are extracted according to the vector relationship in (16), whose amplitude and frequency are $I_{wk\pm}$ and $6k\omega_g/x(x>1)$, respectively. Hence, the grid harmonics at $(6k-1)\omega_g$ and $(6k+1)\omega_g$ can be controlled directly through adjusting $i_{\mathrm{fe}(wk-)}$ and $i_{\mathrm{fe}(wk+)}$, respectively

$$i_{\mathrm{fe}(wk\pm)} = I_{wk\pm}\sin[6k(\omega_g t+\varphi_{\mathrm{ad}})/x+\varphi_{wk\pm}] \quad (17)$$

where φ_{ad} is the additional phase to adjust the feature extraction.

With the imaginary part of (16), $i_{\mathrm{fe}(wk\pm)}$ can be regarded as the sum of the ideal feature signals $i_{\mathrm{fe}(mk\pm)}$ and $i_{\mathrm{fe}(hk\pm)}$ related to the mean value and harmonics of i_L, respectively

$$\begin{aligned} i_{\mathrm{fe}(wk\pm)} &= \frac{2\sqrt{3}}{\pi}\left[i_{\mathrm{fe}(mk\pm)}+i_{\mathrm{fe}(\mathrm{hk}\pm)}\right] \\ &= \frac{2\sqrt{3}}{\pi}\left\{\pm\frac{I_{L,0}}{6k\pm1}\cos\left[6k\left(\omega_g t+\varphi_{\mathrm{ad}}\right)/x\right]\right. \\ &\quad + M_{6k\pm}I_{L,k}\sin\left[6k(\omega_g t+\varphi_{\mathrm{ad}})/x\right. \\ &\quad \left.\left.+\varphi_{6k\pm}\right]/(12k\pm1)\right\}. \end{aligned} \quad (18)$$

Hence, the amplitude of $i_{\mathrm{fe}(hk\pm)}$ is proportional to that of $i_{L,k}$. To eliminate the frequency error between $i_{\mathrm{fe}(hk\pm)}$ and $i_{L,k}$, the mapping from the high frequency $6k\omega_g$ to low frequency $6k\omega_g/x$ can be expressed as

$$\begin{aligned} i_{\mathrm{fe}(hk\pm)} &= \frac{M_{6k\pm}}{12k\pm1}\left[\cos\theta_{ch(k/x)\pm} \quad \sin\theta_{ch(k/x)\pm}\right] \\ &\quad \times\begin{bmatrix} I_{L,k}\sin\left(6k\omega_g t+\varphi_{Lk}\right) \\ I_{L,k}\cos\left(6k\omega_g t+\varphi_{Lk}\right)\end{bmatrix} \end{aligned} \quad (19)$$

where $\theta_{ch(k/x)\pm}$ is the adjusting angle of the frequency mapping.

Hence, $i_{\mathrm{fe}(hk\pm)}$ can be generated from $i_{L,k}$ according to (20)

$$\begin{aligned} i_{\mathrm{fe}(hk\pm)} &= M_{6k\pm}\left[\cos\theta_{ch(k/x)\pm}+\sin\theta_{ch(k/x)\pm}d\left(\cdot\right)/6k\omega_g dt\right] \\ &\quad \times i_{L,k}/\left(12k\pm1\right). \end{aligned} \quad (20)$$

And the adjusting angle $\theta_{ch(k/x)\pm}$ can be expressed as

$$\begin{aligned} \theta_{ch(k/x)\pm} &= 6k(\omega_g t+\varphi_{\mathrm{ad}})/x+\varphi_{6k\pm}-(6k\omega_g t+\varphi_{Lk}) \\ &= \arcsin\frac{(6k\pm1)\sin\varphi_{erk}}{M_{6k\pm}}-\varphi_{erk} \\ &\quad -6k\theta_g\left(1-\frac{1}{x}\right)+\frac{6k\left(\varphi_{\mathrm{ad}}-\varphi\right)}{x}. \end{aligned} \quad (21)$$

As can be seen in Fig. 8, the angle $\theta_g=\omega_g t+\varphi$ of the grid-line voltage can be obtained directly with the analog sampling circuit at the grid side. As the additional phase φ_{ad} is set as φ, the coefficient $6k(\varphi_{\mathrm{ad}}-\varphi)/x$ is equal to 0, which means that $i_{\mathrm{fe}(hk\pm)}$ can be extracted with the dc-side harmonic $i_{L,k}$, the grid angle θ_g, and the phase error φ_{erk}. Meanwhile, $i_{\mathrm{fe}(mk\pm)}$ can be extracted with the mean value $I_{L,0}$ and the grid angle θ_g, which can reduce the computational burden of the feature extraction.

The comparison of the feature signals and resonant component of the grid current is shown in Fig. 10. With the high-to-low frequency mapping in (19), $i_{\mathrm{fe}(wk_r\pm)}$ can characterize the high-frequency resonance at the grid side, which decouples the grid- and dc-side currents.

The frequency of $i_{\mathrm{fe}(wk_r\pm)}$ can be reduced to get away from the resonant frequency ω_{re} through increasing x. From the dash dot line in Fig. 3, the amplitude and phase of $\Delta\boldsymbol{K}_m$ are decreased

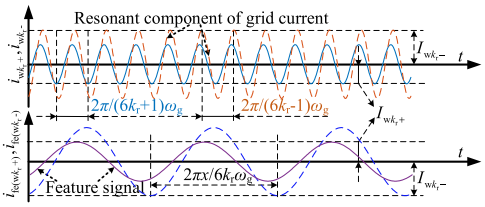

Fig. 10. Comparison of the grid current harmonics and the feature signals.

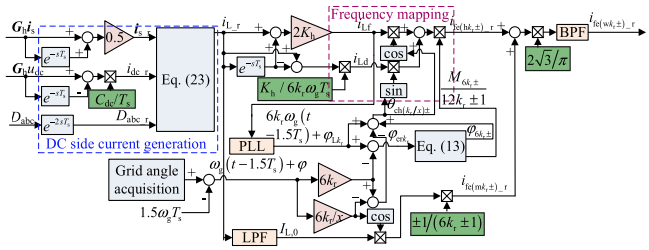

Fig. 11. Block diagram of the generation of the feature signals.

with the input frequency, which means that the frequency mapping can reduce the decay of the feature signal of the resonant component caused by the low dc-link inductance.

B. Control Loop of the Resonance Suppression

The block diagram of the generation of the feature signals is shown in Fig. 11. In order to increase the accuracy of the feature extraction, the phase delays of the applied variables ($\boldsymbol{i}_s$, $u_{\rm dc}$, and D_{abc}) need to be the same, which are set as T_s

$$\begin{cases} \boldsymbol{i}_{s\_r} = 0.5(1+e^{-sT_s})\boldsymbol{G}_h\boldsymbol{i}_s \approx e^{-0.5sT_s}\boldsymbol{G}_h\boldsymbol{i}_s \\ \quad\quad = e^{-sT_s}\left|\boldsymbol{G}_h\right|\boldsymbol{i}_s \\ i_{\rm dc\_r} = C_{\rm dc}(1-e^{-sT_s})\boldsymbol{G}_h u_{\rm dc}/T_s \approx se^{-0.5sT_s}C_{\rm dc}\boldsymbol{G}_h u_{\rm dc} \\ \quad\quad = e^{-sT_s}\left|\boldsymbol{G}_h\right| i_{\rm dc} \end{cases} \tag{22}$$

where $\boldsymbol{i}_{s\_r}$ and $i_{\rm dc\_r}$ are the motor current and the adjusted dc-link current, respectively. $i_{\rm dc}$ is the actual dc-link current.

The duty cycle generated in the FOC is applied at the next switching cycle. Hence, the duty cycle in the reconstruction process should be delayed two switching cycles [19]. Hence, the reconstructed dc-side current i_{L_r} can be presented as

$$\begin{aligned} i_{L\_r} &= e^{-0.5sT_s}\boldsymbol{G}_h sC_{\rm dc}u_{\rm dc} + (D_{a\_r}i_{a\_r} + D_{b\_r}i_{b\_r} \\ &\quad + D_{c\_r}i_{c\_r}) = e^{-sT_s}\left|\boldsymbol{G}_h\right| i_L \end{aligned} \tag{23}$$

where $i_{(abc)\_r}$ is the component of $\boldsymbol{i}_{s\_r}$ on the abc-axis. $D_{(abc)\_r}$ is the duty cycle with the delay of two switching cycles.

From (23), the reconstruction can characterize the same amplitude information of the actual dc-side current i_L. The phase information in i_{L_r} is delayed by one switching cycle.

From (19), the quadrature signal of the dc-side current harmonics at $6k_r\omega_g$ is required for the feature extraction. In the algorithm, the quadrature signal i_{Ld} is obtained from the reconstructed dc-side current i_{L_r}. The harmonics i_{Ld,k_r} near the resonance frequency can be expressed as

$$\begin{aligned} i_{Ld,k_r} &= \boldsymbol{L}^{-1}\left[K_h(1-e^{-sT_s})i_{L\_r,k_r}/6k_r\omega_g T_s\right] \\ &= I_{L,k_r}\cos\left[6k_r\omega_g(t-1.5T_s)+\varphi_{Lk_r}\right] \end{aligned} \tag{24}$$

where i_{L_r,k_r} is the resonant harmonic of i_{L_r}, $\boldsymbol{L}^{-1}(\cdot)$ is the inverse Laplace transformation, and K_h is the compensation gain

$$K_h = 1/|\boldsymbol{G}_h(j6k_r\omega_g)| = 1/|(1-e^{-j6k_r\omega_g T_s})/j6k_r\omega_g T_s|. \tag{25}$$

From (24), the phase delay between i_{Ld,k_r} and actual dc-side harmonics at the same frequency is $1.5T_s$, and the amplitude decay is compensated. To ensure the precision, the phase delays of the applied dc-side current should be the same. Hence, the adjusted dc-side current i_{Lf} is obtained, whose harmonics i_{Lf,k_r} can be expressed as

$$\begin{aligned} i_{Lf,k_r} &= \boldsymbol{L}^{-1}\left[0.5K_h(1+e^{-sT_s})i_{L\_r,k_r}\right] \\ &= I_{L,k_r}\sin\left(6k_r\omega_g t+\varphi_{Lk_r}-9k_r\omega_g T_s\right). \end{aligned} \tag{26}$$

The harmonics i_{Lf,k_r} and i_{Ld,k_r} near the resonance frequency are the input signals of the high-to-low frequency mapping in (19). The adjusting angle $\theta_{ch(k_r/x)\pm}$ in the software algorithm can be generated from the grid angle with the delay of T_m and the angle of i_{Lf,k_r} from the phase-locked loop (PLL)

$$\begin{aligned} \theta_{ch(k_r/x)\pm} &= 6k_r\left[\omega_g(t-T_m)+\varphi\right]/x + \varphi_{6k_r\pm} \\ &\quad - \left[6k_r\omega_g(t-1.5T_{\rm s})+\varphi_{Lk_r}\right] \\ &= \arcsin\left[(6k_{\rm r}\pm1)\sin\varphi_{erk_r}/M_{6k_r\pm}\right] \\ &\quad - \varphi_{erk_r} + 6k_r\omega_g(1.5T_s-T_m) \\ &\quad - 6k_{\rm r}(1-1/x)\left[\omega_g(t-T_m)+\varphi\right]. \end{aligned} \tag{27}$$

As the delay T_m of the grid angle is set as $1.5T_s$, the component $6k\omega_g(1.5T_s-T_m)$ in (27) is equal to 0, and φ_{erk} can be obtained from the error between the grid angle and the angle of i_{Lf,k_r} with the same delay $1.5T_s$, which can be applied to generate the amplitude ratio $M_{6k_r\pm}$. The mean value of i_L can be extracted with the lowpass filter (LPF). With the delayed grid angle, the compensated feature signal $i_{{\rm fe}(mk\pm)\_r}$ related to $I_{L,0}$ is extracted from (18). The compensated feature signal $i_{{\rm fe}(hk\pm)\_r}$ related to $i_{L,k}$ is extracted with the frequency mapping, and the compensated feature signals $i_{{\rm fe}(wk_r-)\_r}$ and $i_{{\rm fe}(wk_r+)\_r}$ are obtained with the bandpass filter (BPF) whose center frequencies are $6\omega_g$ and $12\omega_g$, respectively. The phase delays of $i_{{\rm fe}(wk\pm)\_r}$, $i_{{\rm fe}(mk\pm)\_r}$, and $i_{{\rm fe}(hk\pm)\_r}$ are $1.5T_s$

$$\begin{cases} i_{{\rm fe}(wk_r-)\_r} = \boldsymbol{L}^{-1}\left[e^{-1.5sT_s}i_{{\rm fe}(wk_r-)}\right] \\ \quad = \left[-I_{L,0}\cos 6\left(\theta_g-1.5\omega_g T_s\right)/(6k_r-1)\right. \\ \left.+M_{6k_r-}\left(\cos\theta_{ch1\pm}i_{Lf,k_r}+\sin\theta_{ch1\pm}i_{Ld,k_r}\right)/(12k_r-1)\right] \\ \quad\quad \cdot 2\sqrt{3}/\pi \\ i_{{\rm fe}(wk_r+)\_r} = \boldsymbol{L}^{-1}\left[e^{-1.5sT_s}i_{{\rm fe}(wk_r+)}\right] \\ \quad = \left[I_{L,0}\cos 12\left(\theta_g-1.5\omega_g T_s\right)/(6k_r+1)\right. \\ \left.+M_{6k_r+}\left(\cos\theta_{ch2\pm}i_{Lf,k_r}+\sin\theta_{ch2\pm}i_{Ld,k_r}\right)/(12k_r+1)\right] \\ \quad\quad \cdot 2\sqrt{3}/\pi \end{cases} \tag{28}$$

The amplitude of $i_{\mathrm{fe}(wk_r\pm)\_r}$ is equal to the grid harmonics at $(6k_r \pm 1)\omega_g$. The amplitudes and phases of $i_{\mathrm{fe}(wk_r-)\_r}$ and $i_{\mathrm{fe}(wk_r+)_r}$need to be further adjusted to improve the suppression ability, which applies the additional components $\boldsymbol{M}_{d-}$ and $\boldsymbol{M}_{d+}$

$$\begin{cases} \boldsymbol{M}_{d-} = K_1(\cos\varphi_{d\_1} + \sin\varphi_{d\_1}\cdot s/6\omega_g) \\ \boldsymbol{M}_{d+} = K_2(\cos\varphi_{d\_2} + \sin\varphi_{d\_2}\cdot s/12\omega_g) \end{cases} \tag{29}$$

where K_1, K_2, φ_{d_1}, and φ_{d_2} are the adjusting coefficient and phases for $i_{\mathrm{fe}k_r-}$ and $i_{\mathrm{fe}k_r+}$.

As seen in Fig. 10, the feature signal is a periodic sinusoidal signal. According to [7], the closed loop of $i_{\mathrm{fe}(wk_r\pm)\_r}$ applies the proportional–resonant (PR) controller to increase the control performance. The resonant frequencies are set as $6\omega_g$ and $12\omega_g$

$$\boldsymbol{G}_{\mathrm{PR}} = K_p + \frac{6K_{r1}\xi_1\omega_g s}{s^2 + 6\xi_1\omega_g s + 36\omega_g^2} + \frac{12K_{r2}\xi_2\omega_g s}{s^2 + 12\xi_2\omega_g s + 144\omega_g^2} \tag{30}$$

where $\boldsymbol{G}_{\mathrm{PR}}$ is the transfer function of the PR controller. K_p, K_{r1}, and K_{r2} are the proportional gain and the resonant gains related to $6\omega_g$ and $12\omega_g$. ξ_1 and ξ_2 are the bandwidths related to $6\omega_g$ and $12\omega_g$, respectively.

In the FOC, the duty cycle is obtained with the space vector pulsewidth modulation, whose reference is u_{dc}. From [6], the additional harmonics at the motor side is generated by the dc-link ripples. Hence, the dc-link voltage can be seen as the input signal of the feature signals. The relationship between the adjusting angle $\Delta\theta_u$ and dc-link voltage Δu_{dc} is expressed as

$$\begin{aligned} \Delta\theta_u &= -\boldsymbol{G}_{\mathrm{PR}}\left(\boldsymbol{M}_{d-} i_{\mathrm{fe}(wk_r-)\_r} + \boldsymbol{M}_{d+} i_{\mathrm{fe}(wk_r+)\_r}\right) \\ &= \boldsymbol{G}_{mad}\Delta u_{\mathrm{dc}} \end{aligned} \tag{31}$$

where $\boldsymbol{G}_{mad}$ is the transfer function from $\Delta\theta_u$ to Δu_{dc}.

As shown in (31), the PR controller output depends on the difference between i_{ref} and $\boldsymbol{M}_{d-} i_{\mathrm{fe}(wk_r-)\_r} + \boldsymbol{M}_{d+} i_{\mathrm{fe}(wk_r+)\_r}$. The reference voltages $u_{\alpha\beta\mathrm{ref}\_r}$ in $\alpha\beta$-axes after control are derived as

$$\begin{bmatrix} u_{\alpha\mathrm{ref}\_r} \\ u_{\beta\mathrm{ref}\_r} \end{bmatrix} = \begin{bmatrix} \cos(\hat{\theta}_e + \Delta\theta_u) & \sin(\hat{\theta}_e + \Delta\theta_u) \\ -\sin(\hat{\theta}_e + \Delta\theta_u) & \cos(\hat{\theta}_e + \Delta\theta_u) \end{bmatrix} \begin{bmatrix} u_{d\mathrm{ref}} \\ u_{q\mathrm{ref}} \end{bmatrix} \tag{32}$$

where $u_{d\mathrm{ref}}$ and $u_{q\mathrm{ref}}$ are the d- and q-axis reference voltages, respectively.

As the position and speed observer converges, the estimated rotor position $\hat{\theta}_e$ is equal to the equivalent sampled position θ_{ee}. According to [6], the equivalent voltage references $u_{d\mathrm{ref}\_r}$ and $u_{q\mathrm{ref}\_r}$ in dq-axes can be expressed as

$$\begin{bmatrix} U_{d\mathrm{ref}\_r,0} + \Delta u_{d\mathrm{ref}\_r} \\ U_{q\mathrm{ref}\_r,0} + \Delta u_{q\mathrm{ref}\_r} \end{bmatrix} = \begin{bmatrix} U_{d\mathrm{ref},0} + \Delta u_{d\mathrm{ref}} - U_{q\mathrm{ref},0}\Delta\theta_u \\ U_{q\mathrm{ref},0} + \Delta u_{q\mathrm{ref}} + U_{d\mathrm{ref},0}\Delta\theta_u \end{bmatrix} \tag{33}$$

where $U_{d,q\mathrm{ref\_r},0}$, $U_{d,q\mathrm{ref},0}$, $\Delta u_{d,q\mathrm{ref}\_r}$, and $\Delta u_{d,q\mathrm{ref}}$ are the averages and the variations of the reference voltages in dq-axes with and without control, respectively.

According to (33), the regulation of the voltage angle is equivalent to inject additional small variations $-U_{q\mathrm{ref},0}\Delta\theta_u$ and $U_{d\mathrm{ref},0}\Delta\theta_u$ into the reference voltage. The introduced voltages contain the harmonics at the frequencies of $6\omega_g$ and $12\omega_g$, which are adopted to reshape the impedance relationship between the grid resonance and the rectified voltage.

C. Parameter Design and Performance Analysis

In order to obtain the optimal control effect, the parameters of adjusting components need to be analyzed. From [6], the transfer functions $\boldsymbol{W}_{dmad}$ and $\boldsymbol{W}_{qmad}$ between the dc-link voltage and stator current in dq-axes are reshaped as

$$\begin{cases} \boldsymbol{W}_{d,qmad} = \boldsymbol{W}_{d,q} + e^{-sT_s}\boldsymbol{G}_{mad}\boldsymbol{W}_{d,qre} \\ \begin{bmatrix} \boldsymbol{W}_{dre} \\ \boldsymbol{W}_{qre} \end{bmatrix} = \frac{1}{\boldsymbol{A}_{2q}\boldsymbol{A}_{1d} - \boldsymbol{A}_{2d}\boldsymbol{A}_{1q}} \begin{bmatrix} -U_{q\mathrm{ref},0}\boldsymbol{A}_{2q} - U_{d\mathrm{ref},0}\boldsymbol{A}_{1q} \\ U_{d\mathrm{ref},0}\boldsymbol{A}_{1d} + U_{q\mathrm{ref},0}\boldsymbol{A}_{2d} \end{bmatrix} \end{cases}. \tag{34}$$

The transfer function of the inverter input admittance $\boldsymbol{Y}_{\mathrm{mad}}$ can be denoted as (35) after applying impedance reshaping

$$\begin{aligned} \boldsymbol{Y}_{\mathrm{mad}} = \boldsymbol{Y}_m + \boldsymbol{Y}_{\mathrm{mre}} = 1.5e^{-sT_s}\boldsymbol{G}_{\mathrm{mad}}\,[&\boldsymbol{W}_{d\mathrm{re}}(U_{d,0} + \omega_e L_d I_{q,0} \\ &+ L_d I_{d,0}s + I_{d,0}R_s) + \boldsymbol{W}_{q\mathrm{re}}\,(U_{q,0} - \omega_e L_q I_{d,0} \\ &+ L_q I_{q,0}s + I_{q,0}R_s)]\,/U_{\mathrm{dc},0} + \boldsymbol{Y}_m \end{aligned} \tag{35}$$

where $\boldsymbol{Y}_{mre}$ is the virtual admittance introduced by the suppression strategy. The transfer function $\boldsymbol{G}_{mad}$ shown in (31) is hard to realize, which means that $\boldsymbol{Y}_{mre}$ should be further simplified to reduce the difficulty of parameter design.

Based on the analysis, $\boldsymbol{L}^{-1}(\Delta\theta_u)$ only contains the harmonics at the frequencies of $6n\omega_g$ ($n = 1, 2$). Different from designing $\boldsymbol{M}_{d-}$ and $\boldsymbol{M}_{d+}$ in a full-frequency band, the amplitude and phase characteristics can be designed separately at specific frequency, which can bring the better harmonic suppression effect [6]. Hence, $\boldsymbol{Y}_{mre}$ can be simplified as

$$\begin{aligned} \boldsymbol{Y}_{\mathrm{mre}} = &\left(Y_{\mathrm{re}1}\cos\varphi_{\mathrm{re}1} + Y_{\mathrm{re}1}\sin\varphi_{\mathrm{re}1}s/6\omega_g\right)\boldsymbol{G}_{\mathrm{BPF1}} \\ &+ \left(Y_{\mathrm{re}2}\cos\varphi_{\mathrm{re}2} + Y_{\mathrm{re}2}\sin\varphi_{\mathrm{re}2}s/12\omega_g\right)\boldsymbol{G}_{\mathrm{BPF2}} \end{aligned} \tag{36}$$

where $\boldsymbol{G}_{\mathrm{BPF1}}$ and $\boldsymbol{G}_{\mathrm{BPF2}}$ are the transfer functions of BPFs for $i_{\mathrm{fe}k_r-}$ and $i_{\mathrm{fe}k_r+}$, respectively. $Y_{\mathrm{re}1}$, $Y_{\mathrm{re}2}$, $\varphi_{\mathrm{re}1}$, and $\varphi_{\mathrm{re}2}$ are the amplitudes and phases of $\boldsymbol{Y}_{mre}$ at the frequencies of $6\omega_g$ and $12\omega_g$.

The characteristics of $\boldsymbol{Y}_{mre}$ at the frequencies of $6\omega_g$ and $12\omega_g$ should be the same before and after the design. Under $i_d = 0$ control, Y_{ren} and φ_{ren} should be set as

$$\begin{cases} Y_{\mathrm{re}n} = 1.5\,|\boldsymbol{G}_{madn}\boldsymbol{M}_{\mathrm{re}n}|/U_{\mathrm{dc},0}, \varphi_{ren} \\ \quad\quad = \angle\boldsymbol{G}_{madn}\boldsymbol{M}_{\mathrm{re}n} - 6n\omega_g T_s \\ \boldsymbol{M}_{\mathrm{re}} = \boldsymbol{W}_{d\mathrm{re}}\,(U_{d,0} + \omega_e L_d I_{q,0}) \\ \quad\quad + \boldsymbol{W}_{q\mathrm{re}}\,(U_{q,0} + I_{q,0}R_s + 6L_q I_{q,0}s) \end{cases}. \tag{37}$$

In (37), $\boldsymbol{M}_{\mathrm{re}n}$ and $\boldsymbol{G}_{\mathrm{mad}n}$ represent $\boldsymbol{M}_{\mathrm{re}}(j6n\omega_g)$ and $\boldsymbol{G}_{\mathrm{mad}}(j6n\omega_g)$, respectively. From (37), $\boldsymbol{W}_{d\mathrm{re}}$ and $\boldsymbol{W}_{q\mathrm{re}}$ are related to the system parameters and operation conditions, which means that the design of $\boldsymbol{G}_{\mathrm{mad}n}$ is essential to reduce the grid

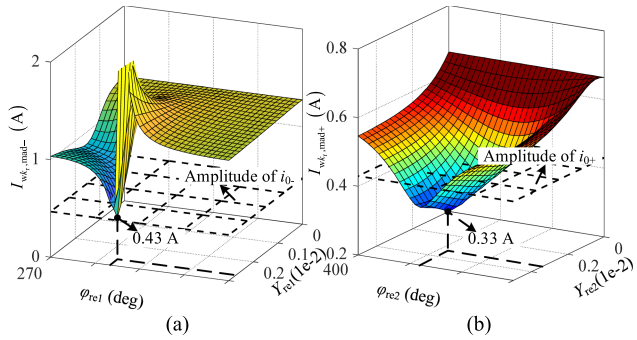

Fig. 12. Grid harmonic amplitudes near *LC* resonant frequency with different values of $Y_{\rm ren}$ and $\varphi_{\rm ren}$ ($n = 1, 2$). (a) At $(6k_r - 1)\omega_g$. (b) At $(6k_r + 1)\omega_g$.

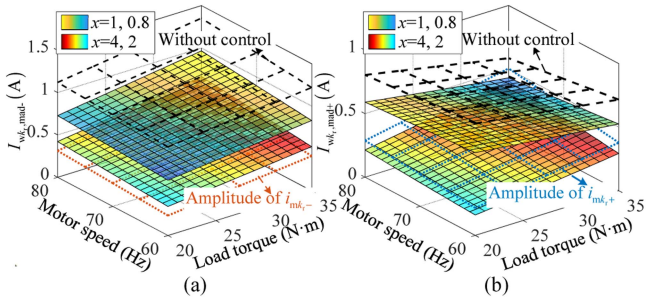

Fig. 13. Resonant component of the grid current under different operating conditions with high- and low-frequency coefficients of the proposed resonance suppression strategy. (a) At $(6k_r - 1)\omega_g$. (b) At $(6k_r + 1)\omega_g$.

current amplitude caused by the resonance

$$\begin{cases} \boldsymbol{G}_{\rm mad1}U_{\rm dc,1}e^{j\varphi_{\rm dc1}} = -(K_p + K_{r1})K_1 I_{wk_r,{\rm mad}-} \\ \qquad\qquad \times e^{j(\varphi_{d\_1}+\varphi_{wk_r,{\rm mad}-}+6\varphi-9\omega_g T_s)} \\ \boldsymbol{G}_{\rm mad2}U_{\rm dc,2}e^{j\varphi_{\rm dc2}} = -(K_p + K_{r2})K_2 I_{wk_r,{\rm mad}+} \\ \qquad\qquad \times e^{j(\varphi_{d\_2}+\varphi_{wk_r,{\rm mad}+}+12\varphi-18\omega_g T_s)} \end{cases} \tag{38}$$

where $I_{wk,{\rm mad}\pm}$ is the amplitude of the grid current with control at $(6k \pm 1)\omega_g$. $\varphi_{wk,{\rm mad}\pm}$ is the phase difference between the grid current and the rectified voltage related to $6k\omega_g$ with control.

From (35), the transfer functions among the dc-side current, dc-link voltage, and rectified voltage $\boldsymbol{K}_{\rm mad}$ and $\boldsymbol{K}_{u\rm mad}$ after control are expressed as

$$\begin{cases} \boldsymbol{K}_{\rm mad} = \Delta i_L/\Delta u_{\rm grec} = 1/\left[1/\left(\boldsymbol{Y}_m + \boldsymbol{Y}_{m\rm re} + C_{\rm dc}s\right)\right. \\ \qquad\qquad \left. + L_{\rm dc}s + R_g\right] \\ \boldsymbol{K}_{u\rm mad} = \Delta u_{\rm dc}/\Delta u_{\rm grec} = 1/\left[1 + \left(L_{\rm dc}s + R_g\right)\right. \\ \qquad\qquad \left. \times \left(\boldsymbol{Y}_m + \boldsymbol{Y}_{m\rm re} + C_{\rm dc}s\right)\right] \end{cases}. \tag{39}$$

Hence, $I_{wk,{\rm mad}\pm}$ and $\varphi_{wk,{\rm mad}\pm}$ can be expressed as

$$\begin{cases} I_{wk,{\rm mad}\pm} = \dfrac{2\sqrt{3}}{\pi}\sqrt{\left[\dfrac{6M_{6k,{\rm mad}\pm}|\boldsymbol{K}_{\rm madk}|U_g\sin\varphi_{6k,{\rm mad}\pm}}{\pi(36k^2-1)(12k\pm1)} \pm \dfrac{I_{L,0}}{6k\pm1}\right]^2 + \left[\dfrac{6M_{6k,{\rm mad}\pm}|\boldsymbol{K}_{\rm madk}|U_g\cos\varphi_{6k,{\rm mad}\pm}}{\pi(36k^2-1)(12k\pm1)}\right]^2} \\ \varphi_{wk,{\rm mad}\pm} = \angle\left(\pm j\dfrac{I_{L,0}}{6k\pm1} + \dfrac{6M_{6k,{\rm mad}\pm}U_g|\boldsymbol{K}_{\rm madk}|}{\pi(36k^2-1)(12k\pm1)}e^{j\varphi_{6k,{\rm mad}\pm}}\right) \end{cases} \tag{40}$$

where $\boldsymbol{K}_{{\rm mad}\,k}$ represents $\boldsymbol{K}_{\rm mad}(j6k\omega_g)$

$$\begin{cases} M_{6k,{\rm mad}\pm} \\ \quad = \sqrt{36k^2 + (\pm12k+1)\sin^2\left(\angle\boldsymbol{K}_{\rm madk} - \pi/2\right)} \\ \varphi_{6k,{\rm mad}\pm} = \arcsin\left[(6k\pm1)\right. \\ \quad \left.\times\sin\left(\angle\boldsymbol{K}_{\rm madk} - \pi/2\right)/M_{6k,{\rm mad}\pm}\right] \end{cases}. \tag{41}$$

From (40), the adjusting coefficient and phases K_n and φ_{d_n} can be designed through analyzing the amplitudes of resonant components $I_{{\rm wk}_r,{\rm mad}-}$ and $I_{{\rm wk}_r,{\rm mad}+}$ at the grid side. The harmonic amplitude $I_{{\rm wk}_r,{\rm mad}-}$ under different values of $Y_{\rm re1}$ and $\varphi_{\rm re1}$ is shown in Fig. 12(a). $I_{wk_r,{\rm mad}-}$ is reduced from 1.14 to 0.43 A when $Y_{\rm re1}$ and $\varphi_{\rm re1}$ are set as 2.7e-3 and 210°, respectively. The harmonic amplitude $I_{{\rm wk}_r,{\rm mad}+}$ with different amplitudes and phases of $\boldsymbol{Y}_{m\rm re}$ at $12\omega_g$ are demonstrated in Fig. 12(b). $I_{wk_r,{\rm mad}+}$ is decreased from 0.75 to 0.33 A when $Y_{\rm re2}$ and $\varphi_{\rm re2}$ are set as 3.5e-3 and 335°, respectively, which illustrates that the control method can reduce the harmonic of the grid current at $(6k_r - 1)\omega_g$ and $(6k_r + 1)\omega_g$, effectively.

With the designed $Y_{\rm ren}$ and $\varphi_{\rm ren}$, the amplitudes and phases of $\boldsymbol{K}_{\rm mad}$ and $\boldsymbol{K}_{u\rm mad}$ at $6\omega_g$ and $12\omega g$ can be obtained. From (37)–(39), the adjusting coefficient and phases of $\boldsymbol{M}_{d-}$ and $\boldsymbol{M}_{d+}$ can be derived as

$$\begin{cases} K_1 = 4U_{\rm dc,0}Y_{\rm re1}U_g\left|\boldsymbol{K}_{u\rm mad1}\right|/ \\ \qquad 35\pi\left[I_{wk_r,{\rm mad}-}\left|\boldsymbol{M}_{\rm re1}\right|\left(K_p + K_{r1}\right)\right] \\ \varphi_{d\_1} = \varphi_{\rm re1} + \angle\boldsymbol{K}_{u\rm mad1} + \pi/2 + 15\omega_g T_s \\ \qquad -\angle\boldsymbol{M}_{\rm re1} - \varphi_{wk_r,{\rm mad}-} \\ K_2 = 4U_{\rm dc,0}Y_{\rm re2}U_g\left|\boldsymbol{K}_{u\rm mad1}\right|/ \\ \qquad 143\pi\left[I_{wk_r,{\rm mad}+}\left|\boldsymbol{M}_{\rm re2}\right|\left(K_{\rm p} + K_{\rm r2}\right)\right] \\ \varphi_{d\_2} = \varphi_{\rm re2} + \angle\boldsymbol{K}_{u\rm mad2} + \pi/2 + 30\omega_g T_s \\ \qquad -\angle\boldsymbol{M}_{\rm re2} - \varphi_{wk_r,{\rm mad}+} \end{cases} \tag{42}$$

where $\boldsymbol{K}_{u{\rm mad}\,n}$ represents $\boldsymbol{K}_{u\rm mad}(j6n\omega_g)$ ($n = 1, 2$).

Fig. 13 shows the harmonic amplitudes of the grid current under different operation conditions with high- and low-frequency coefficients. With the designed coefficients ($Y_{\rm re1}$ = 2.7e-3 and $\varphi_{\rm re1} = 210°$), $I_{{\rm wk}_r,{\rm mad}-}$ can be reduced effectively under the frequency coefficient of 4 and 2. Specifically, the harmonic amplitude at $(6k_r - 1)\omega_g$ can be reduced from 1.13 to 0.52 A under the speed and torque of 75 Hz and 30 N·m, which is 0.30 A lower than the result under the frequency coefficients of 1 and 0.8, respectively. As shown in Fig. 13(b), the amplitudes of the grid current at $(6k_r + 1)\omega_g$ can also be reduced more effectively with the high-frequency coefficient. Meanwhile, the difference between $I_{w4,{\rm mad}\pm}$ and the amplitude of $i_{mk\pm}$ does not exceed 0.03 A. The deterioration of high-frequency resonance on the grid current is almost eliminated under the coupling between the grid- and dc-side currents. Meanwhile, the proposed resonance suppression method can work effectively through improving the frequency coefficient in a wide speed and torque region.

As there exist faults or sensing errors in the motor current sensors, the reconstructed dc-side current is introduced into additional deviation $I_{\rm de,0}$ and $i_{{\rm de},k}$ of the mean value and the small-signal variation at $6k\omega_g$, respectively. Hence, the reconstructed dc-side current i_{L_e} with the deviation can be expressed

as

$$\begin{aligned} i_{L\_e} &= I_{L\_e,0} + \sum_{k=1}^{\infty} i_{L\_e,k} \\ &= I_{L\_e,0} + \sum_{k=1}^{\infty} I_{L\_e,k} \sin\left(6k\omega_g t + \varphi_{L\_ek}\right) \\ &= i_{L\_r} + I_{\mathrm{de},0} + \sum_{k=1}^{\infty} i_{\mathrm{de},k} \\ &= i_{L\_r} + I_{\mathrm{de},0} + \sum_{k=1}^{\infty} I_{\mathrm{de},k} \sin\left(6k\omega_g t + \varphi_{\mathrm{de}k}\right) \end{aligned} \tag{43}$$

where $I_{L\_e,0}$ and $i_{L\_e,k}$ are the mean value and the harmonic of the dc-side current with the deviation at $6k\omega_g$, respectively. $I_{\mathrm{de},k}$ and $\varphi_{\mathrm{de}k}$ are the amplitude and the phase of $i_{L\_e,k}$, respectively. $I_{\mathrm{de},k}$ and $\varphi_{\mathrm{de}k}$ are the amplitude and the phase of $i_{\mathrm{de},k}$, respectively.

Under the condition of the faults or sensing errors, the deviated feature signals $i_{\mathrm{fe}(wk_r\pm)\_e}$ are extracted with the grid angle, the mean value $I_{L\_e,0}$, and the resonant component i_{L_e,k_r} of the dc-side current with the deviation

$$\begin{cases} i_{\mathrm{fe}(wk_r-)\_e} \\ \quad = I_{w\_ek_r-}\sin\left[6(\omega_g t+\varphi) - 9\omega_g T_s + \varphi_{w\_ek_r-}\right] \\ \quad = 2\sqrt{3}/\pi \cdot \left\{ -\frac{(I_{L,0}+I_{\mathrm{de},0})\cos[6(\omega_g t+\varphi)-9\omega_g T_s]}{6k_r-1} \right. \\ \qquad \left. + \frac{M_{e6k_r-}K_h I_{L\_e,k_r}\sin[6(\omega_g t+\varphi)-9\omega_g T_s+\varphi_{e6k_r-}]}{12k_r-1} \right\} \\ i_{\mathrm{fe}(wk_r+)\_e} \\ \quad = I_{w\_ek_r+}\sin\left[12(\omega_g t+\varphi) - 18\omega_g T_s + \varphi_{w\_ek_r-}\right] \\ \quad = 2\sqrt{3}/\pi \cdot \{ \frac{(I_{\mathrm{L},0}+I_{\mathrm{de},0})\cos[12(\omega_g t+\varphi)-18\omega_g T_s]}{6k_r+1} \\ \qquad + \frac{M_{e6k_r+}K_h I_{L\_e,k_r}\sin[12(\omega_g t+\varphi)-18\omega_g T_s+\varphi_{e6k_r+}]}{12k_r+1} \} \end{cases} \tag{44}$$

where $I_{w\_ek\pm}$ is the amplitude of the deviated feature signal for the grid current harmonic at $(6k \pm 1)\omega_g$. $\varphi_{w\_ek\pm}$ is the phase difference between the deviated feature signal $i_{\mathrm{fe}(wk\pm)\_e}$ and the rectified voltage harmonics at the frequency of $6k\omega_g/x$.

In (44), $M_{e6k\pm}$ and $\varphi_{e6k\pm}$ are the amplitude ratio $M_{6k\pm}$ and the phase difference $\varphi_{6k\pm}$ with deviation, respectively, which can be obtained with the phase error φ_{er_ek} between $i_{L\_e,k}$ and the rectified voltage harmonics at $6k\omega_g$.

As the system operates stably, the harmonic amplitude $I_{de,k}$ of the varied deviation is much lower than that of the dc-side current. Hence, $M_{e6k\pm}$ and $\varphi_{e6k\pm}$ are equal to $6k_r\pm0.5$ and φ_{er_ek}, respectively. From the vector analysis in (16), the deviation of the feature extraction near the resonance frequency can be approximately expressed as

$$\begin{aligned} I_{wdk_r\pm}e^{j\varphi_{wdk_r\pm}} &= I_{w\_ek\pm}e^{j\varphi_{w\_ek\pm}} - I_{wk\pm}e^{j\varphi_{wk\pm}} \\ &\approx \left[\pm jI_{\mathrm{de},0}/(6k_r \pm 1)\right. \\ &\left. + \frac{(6k_r \pm 0.5)\,K_h I_{\mathrm{de},k_r}}{12k_r \pm 1} e^{j(\varphi_{\mathrm{de}k_r}+6k_r\omega_g T_s - 6k_r\varphi)}\right] \cdot 2\sqrt{3}\Big/\pi \end{aligned} \tag{45}$$

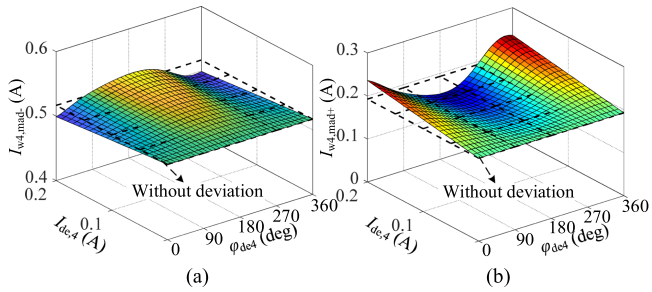

Fig. 14. Resonant components of the grid current under different amplitudes and phases of the dc-side current deviation. (a) At $(6k_r - 1)\omega_g$. (b) At $(6k_r + 1)\omega_g$.

where $I_{wdk\pm}$ is the amplitude of the deviation of the feature extraction related to $(6k \pm 1)\omega_g$. $\varphi_{wdk\pm}$ is the phase difference between the feature extraction deviation and the rectified voltage harmonics related to $6k\omega_g$.

The faults or sensing errors in the motor current sensor reduce the precision of the feature extraction. The deviation of the feature extraction generates the additional angle $\Delta\theta_{\mathrm{de}}$ in the adjusting angle, which can be expressed as

$$\begin{aligned} \Delta\theta_u &= -\boldsymbol{G}_{\mathrm{PR}}\left[\boldsymbol{M}_{d-}i_{\mathrm{fe}(wk_r-)\_e} + \boldsymbol{M}_{d+}i_{\mathrm{fe}(wk_r+)\_e}\right] \\ &= \left(\boldsymbol{G}_{mad} + \boldsymbol{G}_{\mathrm{de}}\right)\Delta u_{\mathrm{dc}} \end{aligned} \tag{46}$$

where $\boldsymbol{G}_{\mathrm{de}}$ is the transfer function from $\Delta\theta_{\mathrm{de}}$ to Δu_{dc}.

From (35), the inverter input admittance $\boldsymbol{Y}_{mad}$ introduces additional admittance $\boldsymbol{Y}_{\mathrm{de}}$ from the feature extraction deviation

$$\begin{aligned} \boldsymbol{Y}_{\mathrm{de}} &= 1.5e^{-sT_s}\boldsymbol{G}_{\mathrm{de}}\boldsymbol{M}_{\mathrm{re}} \\ &\approx \left(Y_{\mathrm{de}1}\cos\varphi_{\mathrm{de}1} + \frac{Y_{\mathrm{de}1}\sin\varphi_{\mathrm{de}1}s}{6\omega_g}\right)\boldsymbol{G}_{\mathrm{BPF1}} \\ &\quad + \left(Y_{\mathrm{de}2}\cos\varphi_{\mathrm{de}2} + \frac{Y_{\mathrm{de}2}\sin\varphi_{\mathrm{de}2}s}{12\omega_g}\right)\boldsymbol{G}_{\mathrm{BPF2}} \end{aligned} \tag{47}$$

where $Y_{\mathrm{de}1}$, $Y_{\mathrm{de}2}$, $\varphi_{\mathrm{de}1}$, and $\varphi_{\mathrm{de}2}$ are the amplitudes and phases of $\boldsymbol{Y}_{\mathrm{de}}$ at the frequencies of $6\omega_g$ and $12\omega_g$.

From (45) and (47), the relationship between the additional admittance $\boldsymbol{Y}_{\mathrm{de}}$ and the feature extraction deviation is expressed as

$$\begin{cases} Y_{\mathrm{de}1}e^{j\varphi_{\mathrm{de}1}} = \frac{35\sqrt{3}\boldsymbol{M}_{\mathrm{re}1}\boldsymbol{M}_{\mathrm{num}1}I_{wdk_r-}e^{j\varphi_{wdk_r-}}}{j2U_g U_{\mathrm{dc},0} - 35\sqrt{3}\boldsymbol{M}_{\mathrm{re}1}\boldsymbol{M}_{\mathrm{den}1}I_{wdk_r-}e^{j\varphi_{wdk_r-}}} \\ Y_{\mathrm{de}2}e^{j\varphi_{\mathrm{de}2}} = \frac{143\sqrt{3}\boldsymbol{M}_{\mathrm{re}2}\boldsymbol{M}_{\mathrm{num}2}I_{wdk_r+}e^{j\varphi_{\mathrm{wdk_r}+}}}{j2U_g U_{\mathrm{dc},0} - 143\sqrt{3}\boldsymbol{M}_{\mathrm{re}2}\boldsymbol{M}_{\mathrm{den}2}I_{wdk_r+}e^{j\varphi_{wdk_r+}}} \\ \boldsymbol{M}_{\mathrm{numn}} = (K_p + K_{rn})K_n e^{j(\varphi_{d\_n} - 15n\omega_g T_s)}/\boldsymbol{K}_{umadn} \\ \boldsymbol{M}_{\mathrm{denn}} = (K_p + K_{rn})K_n e^{j(\varphi_{d\_n} - 15n\omega_g T_s)}(j6nL_{\mathrm{dc}}\omega_g + R_g) \end{cases} \tag{48}$$

With the parameter identification algorithm, the faults or sensing errors do not influence the calculation accuracy of the mean value of the motor voltage and currents in dq-axes, and the additional deviation $I_{\mathrm{de},0}$ can be monitored. Hence, the influence of i_{de,k_r} is discussed in this article.

The resonant components of the grid current under different amplitudes and phases of the dc-side current deviation are shown in Fig. 14. The harmonic amplitudes of the grid current at $(6k_r - 1)\omega_g$ and $(6k_r + 1)\omega_g$ vary in a wide range with different

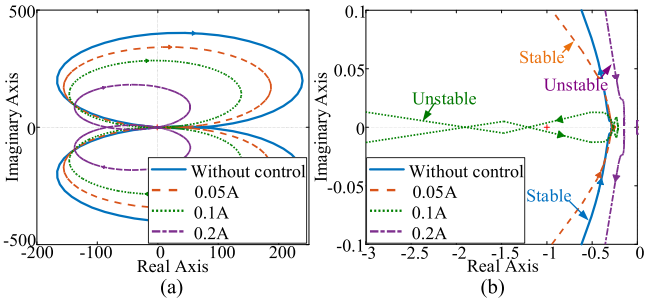

Fig. 15. Nyquist plots of $\boldsymbol{Y}_{mad}/\boldsymbol{Y}_f$ with different amplitudes of the dc-side current deviation. (a) Overall Nyquist plots. (b) Detailed view in (a).

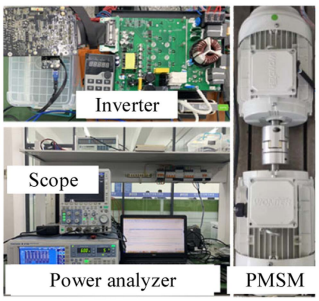

Fig. 16. Experimental platform of the electrolytic capacitorless PMSM drive.

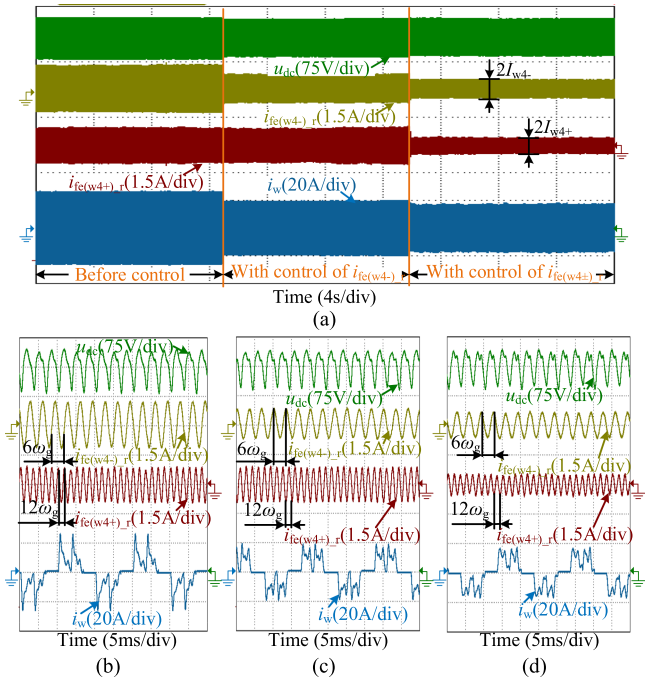

Fig. 17. Experimental results with the proposed resonance suppression method at the motor frequency of 75 Hz. (a) Enable the proposed strategy. (b) Zoomed view without the proposed strategy. (c) Zoomed view with control of $i_{fe(w4-)\_r}$. (d) Zoomed view with control of $i_{fe(w4\pm)\_r}$.

values of $\varphi_{\mathrm{de}k_r}$. For example, $I_{w4,\mathrm{mad}-}$ will increase from 0.52 to 0.53 A when $I_{\mathrm{de},4}$ and $\varphi_{\mathrm{de}4}$ are 0.20 A and 20°, respectively. The situation is revised in $I_{w4,\mathrm{mad}+}$; the harmonic amplitude at $(6k_r+1)\omega_g$ is suppressed from 0.19 to 0.16 A. Even if I_{de,k_r} increases to nearly 40% of I_{L,k_r}, the deviation of the grid current harmonics near the resonant frequency is lower than 0.03 A, which means that the proposed method can maintain the control performance under the faults or sensing errors in the motor current sensors.

The drive system stability can be evaluated by the Nyquist criterion according to the ratio of the *LC* filter impedance and the PMSM impedance. The admittance of the *LC* filter $\boldsymbol{Y}_f$ is

$$\boldsymbol{Y}_f = \left(L_{\mathrm{dc}}C_{\mathrm{dc}}s^2 + R_gC_{\mathrm{dc}}s + 1\right)/\left(L_{\mathrm{dc}}s + R_g\right). \tag{49}$$

The Nyquist plots of $\boldsymbol{Y}_{mmad}/\boldsymbol{Y}_f$ with amplitudes of i_{de,k_r} are shown in Fig. 15. The proposed method can maintain the stability of the drive system when the amplitude is lower than 0.1 A. However, the situation is on the opposite when I_{de,k_r} is too high, and the stability is deteriorated. From Fig. 15, the limit of sensing errors in the motor current sensor is near 0.1 A.

IV. Experimental Results

The proposed strategy is verified on a 5.5-kW electrolytic capacitorless PMSM drive, as shown in Fig. 16. The dc-link capacitance and the line inductance are set as 80 μF and 0.2 mH, respectively, and the *LC* resonant frequency is 1258 Hz ($k_r = 4$). The sampling frequency is 8 kHz. The grid input is 380 Vrms (50 Hz). The motor parameters of L_d, L_q, and R_s are 7.5 mH, 17.2 mH, and 0.265 Ω, respectively. The control algorithms are implemented in a DSP28075 chip.

Fig. 17 shows the experimental results at 75 Hz. The waveforms from the top to the bottom are the dc-link voltage, the feature signals $i_{\mathrm{fe}(w4\pm)\_r}$, and the w-phase grid current. $i_{\mathrm{fe}(w4-)\_r}$ and $i_{\mathrm{fe}(w4+)\_r}$ are the feature signals of the 23th and 25th harmonics in the grid current, respectively. With the control of $i_{\mathrm{fe}(w4-)\_r}$, the peak-to-peak values of the dc-link voltage and the grid current fall from 115.6 V and 53.3 A to 103.1 V and 40.0 A, respectively. After the further control of $i_{\mathrm{fe}(w4+)\_r}$, the peak-to-peak values can be reduced to 96.9 V and 34.6 A. The harmonic amplitudes of the grid current at 1150 and 1250 Hz are decreased from 1.1 and 0.7 A to 0.5 and 0.3 A, respectively.

Fig. 17(b)–(d) shows the zoomed views of the experimental results without and with the proposed strategy. The distortion of the dc-link voltage and the grid current can be suppressed with the method. The frequency coefficient x is set as 4 and 2 for the harmonic suppression at $23\omega_g$ and $25\omega_g$, respectively. Hence, the frequencies of $i_{\mathrm{fe}(w4-)\_r}$ and $i_{\mathrm{fe}(w4+)\_r}$ are set as 300 Hz ($k_r/x = 1$) and 600 Hz ($k_r/x = 2$), respectively, and their amplitudes are equal to the amplitudes of the 23th and 25th harmonics in the grid current, respectively.

Fig. 18(a) and (b) shows the results with the conventional method proposed in [19]. With the optimal parameters, the peak-to-peak values of the dc-link voltage and the grid current are reduced from 115.6 V and 53.3 A to 104.3 V and 46.7 A, respectively. As shown in Fig. 18(b), the peak-to-peak values are varied to 121.9 V and 55.0 A as the conventional method is operated with the general parameters. Comparing the results in Fig. 17(c) with those in Fig. 18(a), the proposed strategy has better suppression performance for high-frequency resonance.

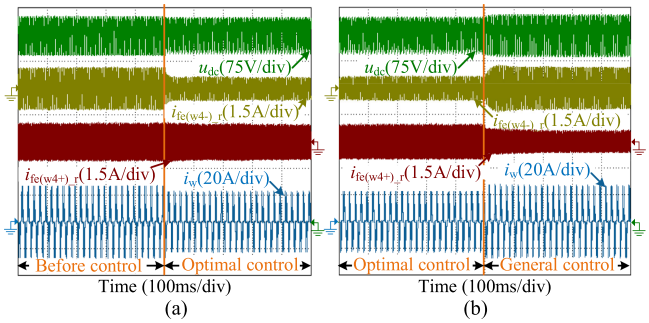

Fig. 18. Experimental results with the conventional method at the motor frequency of 75 Hz. (a) With the optimal parameters. (b) With the general parameters.

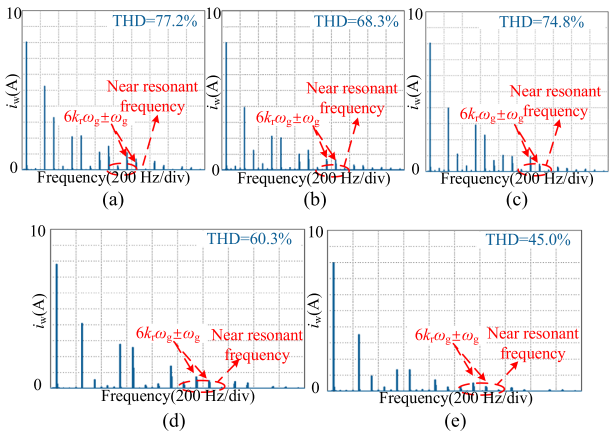

Fig. 19. FFT analysis of the grid current. (a) Without the strategy. (b) With the optimal conventional method. (c) With the general conventional method. (d) With control of $i_{fe(w4-)\_r}$. (e) With control of $i_{fe(w4\pm)\_r}$.

Fig. 19 shows the fast Fourier transform (FFT) analysis of the grid current at the motor frequency of 75 Hz. As shown in Fig. 19(a), the grid current contains the components, caused by the dc-link ripples, at 250, 350, 550, and 650 Hz, and the resonant component at 1150 and 1250 Hz. By comparing Fig. 19(a) and (b), the total harmonic distortion (THD) of the grid current can be reduced by 8.9% with the optimal parameters of the conventional method in [19]. The grid harmonic amplitudes at 1150 and 1250 Hz are reduced from 1.1 and 0.7 A to 0.6 and 0.6 A, respectively. After further increasing the control gain, the grid harmonic amplitude at 1250 Hz is reduced from 0.7 to 0.4 A. However, the harmonic amplitude of the grid current at 1150 Hz is increased from 0.7 to 1.1 A, and the THD of the grid current increases to 74.8% with general control. Hence, the direct extraction of the resonance information at the dc side cannot achieve effective suppression in the drive system with low dc-link inductance.

As can be seen in Fig. 19(d), the resonant components can be effectively suppressed with the proposed method, and the THD can be reduced from 77.2% to 60.3%. Besides, the harmonic amplitudes at 250 and 350 Hz are also decreased from 5.3 and 3.2 A to 4.2 and 0.6 A, respectively. Fig. 19(e) shows the FFT of the grid current with the control of $i_{fe(w4-)\_r}$ and $i_{fe(w4+)\_r}$,

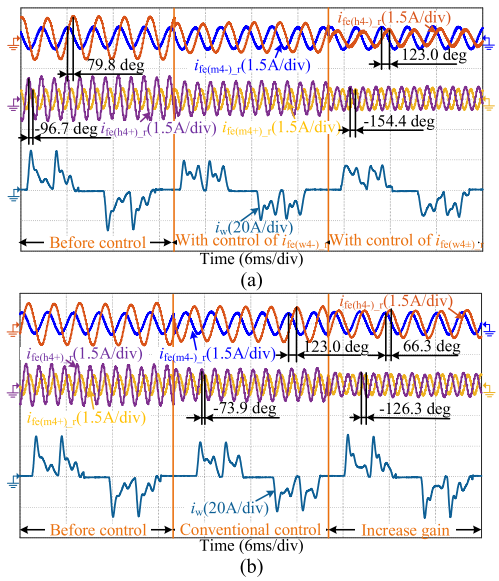

Fig. 20. Experimental results of grid current harmonics. (a) With the proposed method. (b) With the conventional method.

and the THD can be further reduced to 45.0%. The harmonics at 550 and 650 Hz are reduced to 1.5 and 1.4 A, respectively.

Fig. 20(a) shows the influence of the proposed strategy on the grid current harmonics related to the mean value and harmonics of the dc-side current, whose amplitudes are equal to those of $i_{fe(m4\pm)\_r}$ and $i_{fe(h4\pm)\_r}$, respectively. The grid harmonic amplitudes related to the dc-side current at $6k_r\omega_g$ are decreased from 1.1 and 1.0 A to 0.7 and 0.8 A, respectively. Meanwhile, the phase difference between $i_{fe(m4\pm)\_r}$ and $i_{fe(h4\pm)\_r}$ changes from 79.8° and –96.7° to 123.0° and –154.4°. From the vector analysis in Fig. 9, the deterioration effect of $i_{fe(h4\pm)\_r}$ on the grid harmonic amplitude $I_{wk\pm}$ is increased as the phase difference gets close to 0°, which means that the control strategy can reduce the resonant components of the grid current.

Fig. 20(b) shows the effectiveness of the conventional method in [19]. With optimal parameters, $i_{fe(h4-)\_r}$ and $i_{fe(h4+)\_r}$ are suppressed to 0.9 and 0.8 A, respectively, which results in the decrease of 0.4 and 0.1 A in the resonant components of the grid current. Increasing the control gain, the amplitudes of $i_{fe(h4-)\_r}$ and $i_{fe(h4+)\_r}$ are further reduced to 0.7 and 0.6 A, respectively. The suppression effect of *LC* resonance in the dc-side current is improved. However, the phase difference between $i_{fe(m4-)\_r}$ and $i_{fe(h4-)\_r}$ varies from 123.0 to 66.3°, which causes the increase of the deterioration effect of $iL_{,4}$ on the grid current harmonic i_{w4-}. The current coupling between the grid and dc sides worsens the grid harmonic amplitude at 1150 Hz under the conventional method in [19].

To further verify the effectiveness of the strategy, Fig. 21 shows the experimental results at the motor frequency of 60 Hz. The peak-to-peak values of the grid current are reduced from 45.2 to 30.4 A, respectively.

To analyze the implication of the proposed method over the dc side, the dc-link voltage, the actual dc-side current, the reconstructed dc-side current, and the current harmonic at 1200 Hz are shown in Fig. 22. According to the aforementioned analysis,

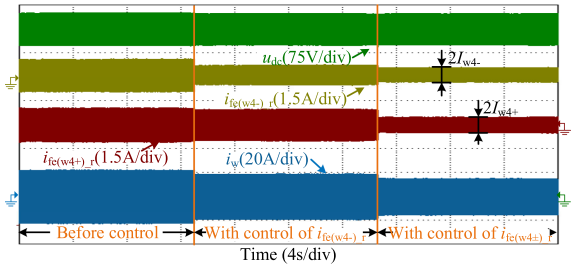

Fig. 21. Experimental results with the proposed resonance suppression method at the motor frequency of 60 Hz.

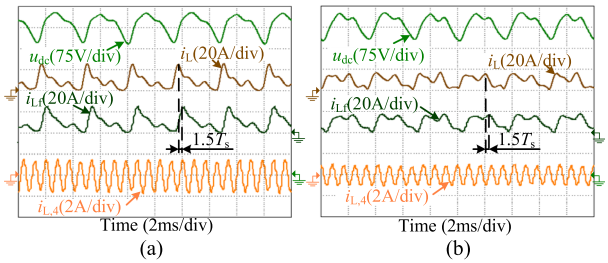

Fig. 22. Implication of the method over the dc-side current. (a) Without the strategy. (b) With the proposed strategy.

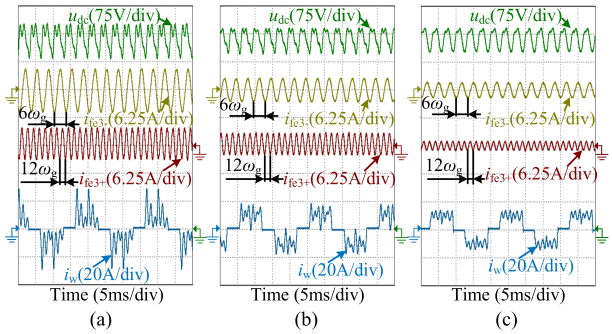

Fig. 23. Experimental results with the proposed resonance suppression method under the grid-line impedance of 0.1 mH. (a) Zoomed view without the proposed strategy. (b) Zoomed view with control of $i_{fe(w3-)\_r}$. (c) Zoomed view with control of $i_{fe(w3\pm)\_r}$.

the resonant component of the dc-side current can be suppressed if the ratio ω_{re}/ω_s is near 0.15. The amplitude of the resonant component in the dc-side current is reduced from 1.4 to 0.9 A. The ripple amplitude of the reconstructed dc-side current i_{Lf} is equal to that of the actual value i_L. The phase delay between i_{Lf} and i_L is delay of $1.5T_s$, which is consistent to the analysis in (26).

In order to verify the robustness of the strategy, the grid-line impedance is set as 0.1 mH, and the resonance frequency is 880 Hz. Fig. 23 shows the experimental results at 75 Hz. As can be seen in Fig. 23(a), the harmonic order k_r of the dc-side current, which is severely affected by *LC* resonance, varies from 4 to 3. The frequencies of compensated feature signals $i_{fe(w3-)\_r}$ and $i_{fe(w3+)\_r}$ are also set as 300 and 600 Hz, respectively, which means that $x = 3, 1.5$. With the control of i_{fe3-}, the peak-to-peak values of the dc-link voltage and the grid current fall from 96.9 V and 58.3 A to 71.8 V and 36.7 A, respectively. After the further

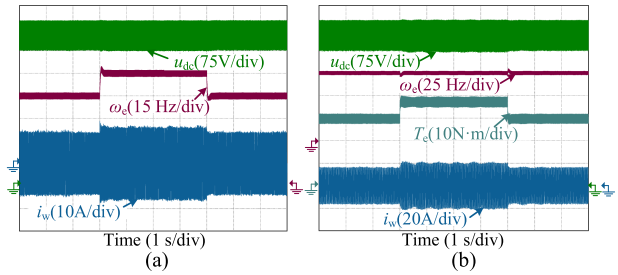

Fig. 24. Dynamic experimental waveforms of the proposed method. (a) Speed dynamic process. (b) Load torque dynamic process.

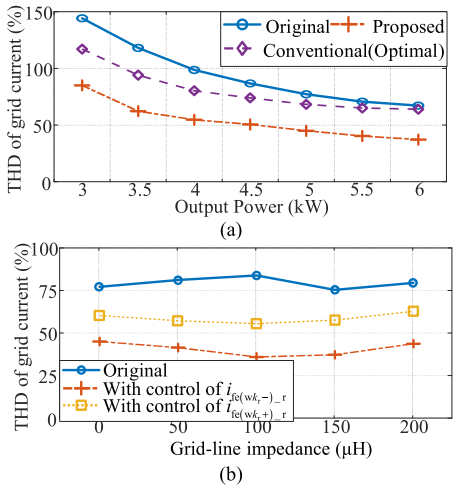

Fig. 25. THD of the grid current. (a) Under different output power conditions. (b) Under different values of grid-line impedances.

control of $i_{fe(w3+)\_r}$, the peak-to-peak values can be reduced to 64.6 V and 29.8 A. The harmonic amplitudes of the grid current at 850 and 950 Hz are decreased from 5.1 and 3.6 A to 2.1 and 0.9 A, respectively. This means that the proposed method maintains the effectiveness under the variations of the ac-side (grid side) impedance.

The experimental waveforms of variable speed operation are shown in Fig. 24(a) when the operation frequency varies from 60 to 75 Hz and back to 60 Hz. The overshoot caused by the step variation of the motor speed is lower than 3 Hz, and the stability of the motor speed is not deteriorated. Fig. 24(b) shows the experimental waveform when the load torque varies between 30 and 37 N·m. The disturbance of motor speed from the torque step variation is lower than 2 Hz. Meanwhile, the amplitude of the resonant component in the grid current remains below 0.7 A during the torque and speed changes. Hence, the proposed method has the tolerance of dynamic performance, and torque and speed ripple.

Fig. 25(a) shows the THD of the grid current under different output power conditions. As the output power increases, the control performance of the conventional method with optimal parameters reduces significantly. With the proposed method, the THD of the grid current can be reduced by more than 30%. The THD of the grid current will satisfy the requirement of IEC-61000-3-12 ($R_{sce} > 350$) if the grid current is higher than 16 A. R_{sce} is the short-circuit ratio of the drive system.

Fig. 25(b) shows the THD of the grid current under different values of grid-line impedances. As the grid-line impedance increases, the THD of the grid-side current can be reduced by more than 30%, which proves the robustness of the strategy to the variations of the ac-side (grid side) impedance.

V. Conclusion

This article studies the high-frequency resonant suppression method in the electrolytic capacitorless drive system with low dc-link inductance. The coupling between the grid- and dc-side currents is analyzed, which shows the difficulty of harmonic suppression through extracting the resonance information from the dc side. On this basis, the low-frequency feature signals of the grid current harmonics are constructed with the dc-side current and the grid voltage phase. An impedance reshaping strategy based on the closed loop of feature signals is proposed. With the high-to-low frequency mapping, the high-frequency resonance information can be controlled directly through the feature signals at the frequencies of 300 and 600 Hz, which suppress the resonant components of the grid current effectively. The experimental results show that the method reduces the harmonic amplitudes of the grid current at 1150 and 1250 Hz by 55% and 58%, respectively. Meanwhile, the THD of the grid-side current is reduced by 32.16%.

References

[1] G. Wu, S. Huang, Q. Wu, F. Rong, C. Zhang, and W. Liao, "Robust predictive torque control of N∗3-phase PMSM for high-power traction application," *IEEE Trans. Power Electron.*, vol. 35, no. 10, pp. 10799–10809, Oct. 2020.

[2] K. Yu and Z. Wang, "Improved deadbeat predictive current control of dual three-phase variable-flux PMSM drives with composite disturbance observer," *IEEE Trans. Power Electron.*, vol. 37, no. 7, pp. 8310–8321, Jul. 2022.

[3] J. Huo, N. Zhao, R. Gao, G. Zhang, G. Wang, and D. Xu, "Analysis and compensation of position estimation error for sensorless reduced DC-link capacitance IPMSM drives," *IEEE Trans. Ind. Electron.*, vol. 70, no. 3, pp. 3213–3221, Mar. 2023.

[4] Y. Son and J. I. Ha, "Direct power control of a three-phase inverter for grid input current shaping of a single-phase diode rectifier with a small DC-link capacitor," *IEEE Trans. Power Electron.*, vol. 30, no. 7, pp. 3794–3803, Jul. 2015.

[5] N. Zhao, R. Gao, G. Wang, D. Ding, G. Zhang, and D. Xu, "Online estimation method of DC-link capacitors for reduced DC-link capacitance IPMSM drives," *IEEE Trans. Power Electron.*, vol. 36, no. 11, pp. 12196–12201, Nov. 2021.

[6] D. Ding et al., "Beatless control strategy based on impedance reshaping for PMSM drives with small DC-link capacitors," *IEEE Trans. Ind. Electron.*, vol. 71, no. 7, pp. 6829–6840, Jul. 2024.

[7] N. Zhao, G. Wang, D. Xu, and D. Xiao, "An active damping control method for reduced DC-link capacitance IPMSM drives," *IEEE Trans. Ind. Electron.*, vol. 65, no. 3, pp. 2057–2068, Mar. 2018.

[8] D. Ding, G. Wang, N. Zhao, G. Zhang, and D. Xu, "An anti-overvoltage control scheme for electrolytic capacitorless IPMSM drives based on stator current vector orientation," *IEEE Trans. Ind. Electron.*, vol. 67, no. 5, pp. 3517–3527, May 2020.

[9] S. Zhu, W. Huang, Y. Yan, and Z. Niu, "High-damped complex vector current regulator for PMSM based on active damping function," *IEEE Trans. Power Electron.*, vol. 38, no. 4, pp. 5204–5216, Apr. 2023.

[10] Y. Chen, Y. Zhang, E. Qu, and M. He, "Active damping method for LC-DAB system based on a power-based impedance model," *IEEE Trans. Power Electron.*, vol. 38, no. 4, pp. 4405–4418, Apr. 2023.

[11] H. Li, Q. Yin, Q. Wang, H. Luo, and Y. Hou, "A novel DC-link voltage feedback active damping control method for IPMSM drives with small DC-link capacitors," *IEEE Trans. Power Electron.*, vol. 69, no. 3, pp. 2426–2436, Mar. 2022.

[12] S. S. Badini and V. Verma, "A new stator resistance estimation technique for vector-controlled PMSM drive," *IEEE Trans. Ind. Appl.*, vol. 56, no. 6, pp. 6536–6545, Nov./Dec. 2020.

[13] H. Shin, Y. Son, and J. I. Ha, "Grid current shaping method with DC-link shunt compensator for three-phase diode rectifier-fed motor drive system," *IEEE Trans. Power Electron.*, vol. 32, no. 2, pp. 1279–1288, Feb. 2017.

[14] I. Won, Y. Cho, and K. B. Lee, "Predictive control algorithm for capacitor-less inverters with fast dynamic response," in *Proc. IEEE Int. Conf. Power Energy*, Melaka, Malaysia, 2016, pp. 479–483.

[15] S. Xuan, Q. Gao, Y. Wang, X. Cai, and L. Luo, "An electrolytic capacitor-less IPMSM drive with input current shaping based on the predictive control," in *Proc. Eur. Conf. Power Electron. Appl.*, Geneva, Switzerland, 2015, pp. 1–7.

[16] H. Chang, S. Lu, G. Huang, S. Zheng, and B. Song, "An extended active resonance suppression scheme based on a dual-layer network for high-performance double-inertia drive system," *IEEE Trans. Power Electron.*, vol. 38, no. 11, pp. 13717–13729, Nov. 2023.

[17] S. Wang et al., "Harmonic resonance suppression with inductive power filtering method: Case study of large- scale photovoltaic plant in China," *IEEE Trans. Power Electron.*, vol. 38, no. 5, pp. 6444–6454, May 2023.

[18] D. Wang, K. Lu, P. O. Rasmussen, L. Mathe, Y. Feng, and F. Blaabjerg, "Voltage modulation using virtual positive impedance concept for active damping of small DC-link drive system," *IEEE Trans. Power Electron.*, vol. 33, no. 12, pp. 10611–10621, Dec. 2018.

[19] D. Ding et al., "Impedance reshaping for inherent harmonics in PMSM drives with small DC-link capacitor," *IEEE Trans. Power Electron.*, vol. 37, no. 12, pp. 14265–14279, Dec. 2022.

[20] X. Xiong, Y. Zhou, B. Luo, P. Cheng, and F. Blaabjerg, "Analysis and suppression strategy of synchronous frequency resonance for grid-connected converters with power-synchronous control method," *IEEE Trans. Power Electron.*, vol. 38, no. 6, pp. 6945–6955, Jun. 2023.

[21] K. Abe, H. Haga, K. Ohishi, and Y. Yokokura, "Direct DC-link current control considering voltage saturation for realization of sinusoidal source current waveform without passive components for IPMSM drives," *IEEE Trans. Ind. Electron.*, vol. 65, no. 5, pp. 3805–3814, May 2018.

[22] K. Abe, H. Haga, K. Ohishi, and Y. Yokokura, "Fine current harmonics reduction method for electrolytic capacitor-less and inductor-less inverter based on motor torque control and fast voltage feedforward control for IPMSM," *IEEE Trans. Ind. Electron.*, vol. 64, no. 2, pp. 1071–1080, Feb. 2017.

[23] K. Li, T. Sun, H. Li, Y. Wang, W. Li, and L. Gong, "Grid current quality improvement for three-phase diode rectifier-fed small DC-link capacitance IPMSM drives," *IEEE Trans. Energy Convers.*, vol. 37, no. 4, pp. 2310–2320, Dec. 2022.

[24] J. Huo, N. Zhao, G. Wang, G. Zhang, L. Zhu, and D. Xu, "An active damping control method for reduced DC-link capacitance PMSM drives with low line inductance," *IEEE Trans. Power Electron.*, vol. 37, no. 12, pp. 14328–14342, Dec. 2022.

[25] G. Zhang et al., "Adaptive step-size predictive PLL based rotor position estimation method for sensorless IPMSM drives," *IEEE Trans. Power Electron.*, vol. 39, no. 5, pp. 6136–6147, May 2024.

[26] G. Zhang et al., "PR internal mode extended state observer-based iterative learning control for thrust ripple suppression of PMLSM drives," *IEEE Trans. Power Electron.*, vol. 39, no. 8, pp. 10095–10105, Aug. 2024.

[27] L. Rovere, A. Formentini, and P. Zanchetta, "FPGA implementation of a novel oversampling dead beat controller for PMSM drives," *IEEE Trans. Ind. Electron.*, vol. 66, no. 5, pp. 3731–3741, May 2019.

[28] X. Huang, X. Ruan, J. Fang, and S. Kan, "A virtual impedance based control scheme for modular electrolytic capacitor-less second harmonic current compensator," *IEEE Trans. Ind. Electron.*, vol. 68, no. 1, pp. 198–209, Jan. 2021.

Runfeng Gao received the B.S. and M.S. degrees in electrical engineering in 2020 and 2022, respectively, from the Harbin Institute of Technology, Harbin, China, where he is currently working toward the Ph.D. degree in power electronics and electrical drives.

His current research interests include advanced control strategies for permanent magnet synchronous motor systems and electrolytic capacitorless drives.

Dawei Ding (Member, IEEE) received the B.S. and M.S. degrees from the Hefei University of Technology, Hefei, China, in 2014 and 2017, respectively, and the Ph.D. degree from the Harbin Institute of Technology (HIT), Harbin, China, all in electrical engineering, in 2021.

Since 2022, he has been a Faculty Member with the School of Electrical Engineering and Automation, HIT, where he is currently an Associate Professor.

Gaolin Wang (Senior Member, IEEE) received the B.S., M.S., and Ph.D. degrees in electrical engineering from the Harbin Institute of Technology, Harbin, China, in 2002, 2004, and 2008, respectively.

In 2009, he joined the Department of Electrical Engineering, Harbin Institute of Technology, as a Lecturer, where he has been a Full Professor of Electrical Engineering since 2014.

Dr. Wang is a Guest Associate Editor for IEEE TRANSACTIONS ON INDUSTRIAL ELECTRONICS and an Associate Editor for IEEE TRANSACTIONS ON TRANSPORTATION ELECTRIFICATION and *IET Electric Power Applications*.

Qiwei Wang (Member, IEEE) received the B.S., M.S., and Ph.D. degrees in electrical engineering from the Harbin Institute of Technology (HIT), Harbin, China, in 2015, 2017, and 2022, respectively.

He is currently an Assistant Professor with the School of Electrical Engineering and Automation, HIT. His current research interests include parameter identification techniques and permanent magnet synchronous motor position sensorless control.

Guoqiang Zhang (Senior Member, IEEE) received the B.S. degree from Harbin Engineering University, Harbin, China, in 2011, and the M.S. and Ph.D. degrees from the Harbin Institute of Technology (HIT), Harbin, in 2013 and 2017, respectively, all in electrical engineering.

Since 2017, he has been a Faculty Member with the School of Electrical Engineering and Automation, HIT, where he is currently a Professor.

Dianguo Xu (Fellow, IEEE) received the B.S. degree in control engineering from Harbin Engineering University, Harbin, China, in 1982, and the M.S. and Ph.D. degrees in electrical engineering from the Harbin Institute of Technology (HIT), Harbin, in 1984 and 1989, respectively.

Since 1994, he has been a Professor with the Department of Electrical Engineering, HIT, where he was the Dean of School of Electrical Engineering and Automation, from 2000 to 2010. From 2014 to 2020, he was the Vice-President of HIT. He has authored or coauthored more than 600 technical papers.

Dr. Xu is the Co-Editor-in-Chief for IEEE TRANSACTIONS ON POWER ELECTRONICS and an Associate Editor for IEEE TRANSACTIONS ON INDUSTRIAL ELECTRONICS and IEEE JOURNAL OF EMERGING AND SELECTED TOPICS IN POWER ELECTRONICS. He is the Chairman of the IEEE Harbin Section.